

## A 205 $\mu\text{m}$ [N II] MAP OF THE CARINA NEBULA

T. E. OBERST<sup>1,4</sup>, S. C. PARSHLEY<sup>1</sup>, T. NIKOLA<sup>1</sup>, G. J. STACEY<sup>1</sup>, A. LÖHR<sup>2,5</sup>, A. P. LANE<sup>2</sup>, A. A. STARK<sup>2</sup>, AND J. KAMENETZKY<sup>3</sup>

<sup>1</sup> Department of Astronomy, Cornell University, Ithaca, NY 14853, USA

<sup>2</sup> Harvard-Smithsonian Center for Astrophysics, Cambridge, MA 02138, USA

<sup>3</sup> Center for Astrophysics and Space Astronomy, University of Colorado, Boulder, CO 80303, USA

Received 2011 April 5; accepted 2011 July 7; published 2011 September 15

### ABSTRACT

We present the results of a  $\sim 250$  arcmin<sup>2</sup> mapping of the 205  $\mu\text{m}$  [N II] fine-structure emission over the northern Carina Nebula, including the Car I and Car II H II regions. Spectra were obtained using the South Pole Imaging Fabry-Perot Interferometer (SPIFI) at the Antarctic Submillimeter Telescope and Remote Observatory (AST/RO) at the South Pole. We supplement the 205  $\mu\text{m}$  data with new reductions of far-IR fine-structure spectra from the *Infrared Space Observatory* (ISO) Long Wavelength Spectrometer (LWS) in 63  $\mu\text{m}$  [O I], 122  $\mu\text{m}$  [N II], 146  $\mu\text{m}$  [O I], and 158  $\mu\text{m}$  [C II]; the 146  $\mu\text{m}$  [O I] data include 90 raster positions which have not been previously published. Morphological comparisons are made with optical, radio continuum, and CO maps. The 122/205 line ratio is used to probe the density of the low-ionization gas, and the 158/205 line ratio is used to probe the fraction of C<sup>+</sup> arising from photodissociation regions (PDRs). The [O I] and [C II] lines are used to construct a PDR model of Carina. When the PDR properties are compared with other sources, Carina is found to be more akin to 30 Doradus than galactic star-forming regions such as Orion, M17, or W49; this is consistent with the view of Carina as a more evolved region, where much of the parent molecular cloud has been ionized or swept away. These data constitute the first ground-based detection of the 205  $\mu\text{m}$  [N II] line, and the third detection overall since those of *COBE* FIRAS and the *Kuiper Airborne Observatory* in the early 1990s.

**Key words:** H II regions – infrared: ISM – ISM: individual objects (Carina Nebula) – ISM: lines and bands – photon-dominated region (PDR) – submillimeter: ISM

*Online-only material:* color figures

### 1. INTRODUCTION

The Carina Nebula (NGC 3372) is a giant diffuse emission nebula in the Carina spiral arm of the Galaxy. It visibly spans  $\sim 2^\circ \times 2^\circ$  in the southern sky, with a nominal center at R.A. =  $10^{\text{h}}44^{\text{m}}$  and decl. =  $-59^\circ53'$  (J2000).

Carina boasts a more impressive concentration of very luminous stars than any other known place in the Galaxy. It is currently powered by UV radiation from 65 O-type stars and 3 WNH stars—including 6 of the 16 known O2- and O3-type stars in the Galaxy—but for most of its lifetime was powered by 70 O-type stars that produced a UV flux 150 times that of the Orion Nebula (Maíz-Apellániz et al. 2004; Smith 2006a). It rivals the 30 Doradus region of the Large Magellanic Cloud (Section 4.6).

The most famous stellar member of Carina is the peculiar Luminous Blue Variable (LBV)  $\eta$  Car, which has a bolometric luminosity of  $L = 10^{6.67} L_\odot$  and mass of  $M \sim 100 M_\odot$  (Smith 2006a), making it one of the most massive and most luminous known stars in the Galaxy. The “Great Eruption” of  $\eta$  Car in the 1840s resulted in the ejection of a dense bipolar nebula called the “Homunculus,” which now obscures the central star. Measurements of the expansion parallax of the Homunculus nebula give a distance to  $\eta$  Car of  $2.3 \text{ kpc} \pm 2\%$  (Allen & Hillier 1993; Smith 2006b), which we take as the distance to the Carina Nebula as a whole in the remainder of this work.

Multi-wavelength studies over the past  $\sim 50$  years have yielded a wealth of information about Carina. The varied nebula

contains prominent H II regions (e.g., Gardner & Morimoto 1968; McGee & Gardner 1968; Huchtmeier & Day 1975; Retallack 1983; Ghosh et al. 1988; Whiteoak 1994; Brooks et al. 2001; Mizutani et al. 2002), photodissociation regions (PDRs; e.g., Zhang et al. 2001; Rathborne et al. 2002; Brooks et al. 2003; Mizutani et al. 2004; Tapia et al. 2006; Kramer et al. 2008), a giant molecular cloud (GMC; e.g., Gardner et al. 1973; Dickel & Wall 1974; Dickel 1974; de Graauw et al. 1981; Brooks et al. 1998, 2003; Zhang et al. 2001; Kramer et al. 2008), and several open clusters (e.g., Feinstein 1995; Walborn 1995; Tapia et al. 2003; Smith 2006a). Recent studies have revealed many of the exciting features associated with active star formation in the nebula, including “elephant trunk” pillars of neutral gas extending into H II regions, visible disks of dust around embedded stars (proplyds), and jets associated with the birth of massive stars (e.g., Megeath et al. 1996; Brooks et al. 2001; Rathborne et al. 2002; Tapia et al. 2003, 2006; Sanchawala et al. 2007a, 2007b; Smith et al. 2010a, 2010b).

At visible wavelengths, the northern part of the nebula forms an arrowhead-shaped nebulosity whose edges are defined by the two prominent (“east” and “west”) dust lanes (Figure 1). This arrowhead region contains two open clusters, Trumpler (Tr) 14 and 16, where the most massive stars of Carina reside ( $\eta$  Car is a member of Tr 16). The strong UV radiation of Tr 14 and 16 powers two prominent H II regions, Car I and II, respectively. The more westerly of these ionized regions, Car I, rests on the eastern edge of a GMC extending  $>20$  pc to the west (and which also partially wraps behind Car I along our line of sight). As evidenced by PDR emission from the surface of the GMC (and many other observed factors), Car I and II can be viewed as expanding bubbles of ionizing radiation actively dissociating and eroding the surfaces of (what remains of) their

<sup>4</sup> Current Address: Department of Physics, Westminster College, New Wilmington, PA 16172, USA; oberste@westminster.edu.

<sup>5</sup> Current Address: Ion Torrent Systems, South San Francisco, CA 94080, USA.

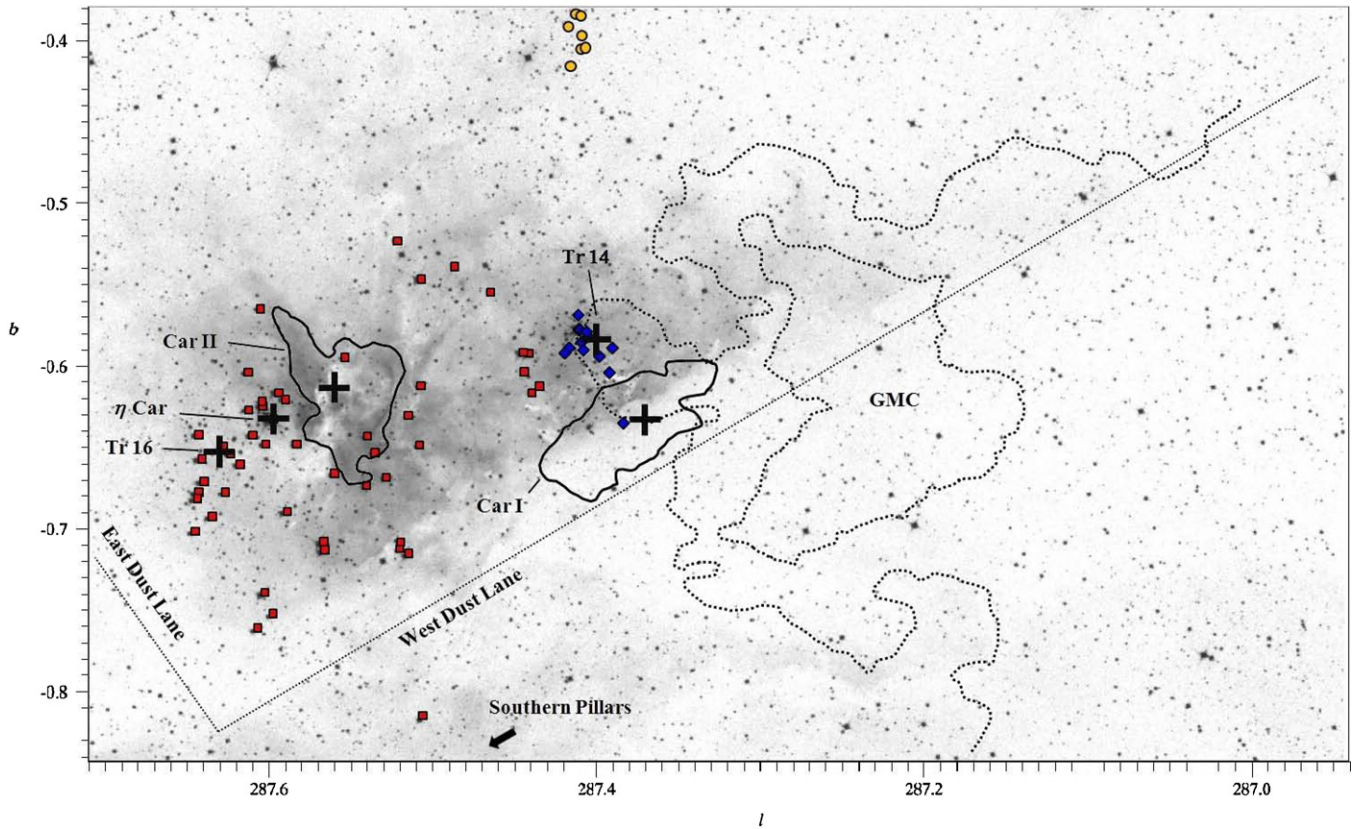


**Figure 1.** Carina Nebula. Drawings of the major components of the Carina Nebula are overlaid on an optical Digital Sky Survey (DSS) inverted-gray-scale photograph (<http://skyview.gsfc.nasa.gov/>; Lasker et al. 1990). Solid contours outline the Car I and II H II regions at  $\sim 50\%$  of peak intensity in 843 MHz (thermal) radio continuum emission (Whiteoak 1994). Dotted contours outline the giant molecular cloud (GMC) at  $\sim 15\%$  and  $30\%$  of peak intensity in 115 GHz  $^{12}\text{CO}(1\rightarrow 0)$  emission (Brooks et al. 1998). OB stars (through B2V) are shown by cluster: Tr 14 in (blue) diamonds, Tr 16 in (red) squares, and Tr 15 in (yellow) circles (Smith 2006a). The centers of the major sources are marked with crosses, as determined by Röser & Bastian (1988) for  $\eta$  Car, Whiteoak (1994) for Car I and II, and Kharchenko et al. (2005) for Tr 14 and 16.

(A color version of this figure is available in the online journal.)

parental clouds, helping to trigger the current generation of star formation.

## 2. OBSERVATIONS

### 2.1. SPIFI Observations

The South Pole Imaging Fabry-Perot Interferometer (SPIFI; Swain et al. 1998; Bradford 2001; Bradford et al. 2002) is a direct-detection imaging spectrometer which operates near the background photon noise limit in the submillimeter (submm;  $\lambda = 200\ \mu\text{m}$ –1 mm) regime. After initial success measuring  $370\ \mu\text{m}$  [CI] and  $^{12}\text{CO}(7\rightarrow 6)$  emission lines from the James Clerk Maxwell Telescope (JCMT) on Mauna Kea (e.g., Bradford et al. 2003, 2005), SPIFI underwent a series of upgrades and modifications to optimize its performance in the  $200\ \mu\text{m}$  window (Oberst 2009) and was installed on the 1.7 m Antarctic Submillimeter Telescope and Remote Observatory (AST/RO; Stark et al. 1997b; Stark et al. 2001) at the South Pole in 2003 December.

SPIFI observed spectra containing the [N II]  $205\ \mu\text{m}$  line (Table 1) in the Carina Nebula during 15 days (August 15–30) of the 2005 Polar winter, as previously reported in Oberst et al. (2006). During these observations, the  $205\ \mu\text{m}$  line-of-sight transmission ranged from 3%–6%, with an average value of 4.5% and standard deviation of 0.7% on  $\sim 1$  day timescales (Oberst 2009).

**Table 1**  
Observed Spectral Lines

Species	Transition	$\lambda$ ( $\mu\text{m}$ ) <sup>a</sup>	Beam ( $''$ ) <sup>b</sup>	$R$ ( $\lambda/\Delta\lambda$ ) <sup>b</sup>
<i>ISO:</i>				
[O I]	$^3P_2 \rightarrow ^3P_1$	63.18372	87.2	223
[N II]	$^3P_2 \rightarrow ^3P_1$	121.8981	78.2	209
[O I]	$^3P_1 \rightarrow ^3P_0$	145.52547	70.0	249
[C II]	$^2P_{3/2} \rightarrow ^2P_{1/2}$	157.7409	70.1	270
<i>SPIFI:</i>				
[N II]	$^3P_1 \rightarrow ^3P_0$	205.1782	54	4250

**Notes.**

<sup>a</sup> The references for  $\lambda$  are  $63\ \mu\text{m}$  [O I], Watson et al. (1984); 122 and  $205\ \mu\text{m}$  [N II], Brown et al. (1994);  $146\ \mu\text{m}$  [O I], Saykally & Evenson (1979); and  $158\ \mu\text{m}$  [C II], Cooksy et al. (1986) and Boreiko et al. (1990).

<sup>b</sup> The *ISO* beam diameters and spectral resolution elements,  $\Delta\lambda$ , have been taken from Gry et al. (2003).

SPIFI mapped two separate areas in the nebula (Figure 2): (1) a  $\sim 14' \times 14'$  area containing the Car I H II region and a portion of the GMC to the south and west, and (2) a  $\sim 12' \times 10'$  area containing the Car II H II region and vicinity to the east. Each pixel in SPIFI's 25 ( $5 \times 5$ ) detector array of Winston cone-fed thermistor-sensed bolometers had a circular beam of  $\sim 54''$  FWHM and the array's inter-beam spacing was  $\sim 65''$ . The entire array ( $\sim 325'' \times 325''$  field of view) was moved



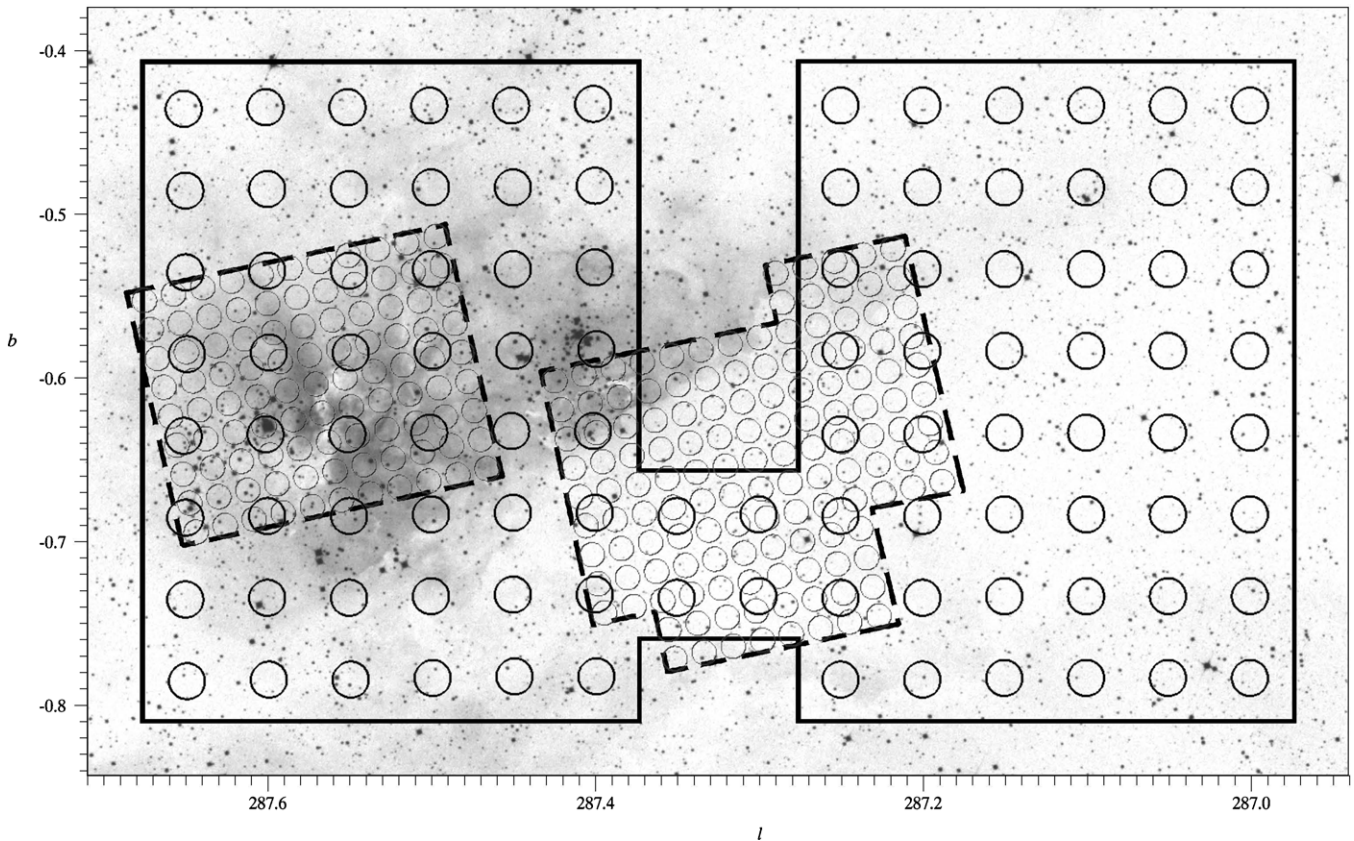


**Figure 2.** SPIFI and ISO Rasters. SPIFI and *ISO* rasters are shown overlaid on the same DSS photograph as in Figure 1. The 100 larger circles (79'' diameter beams, within the solid border) mark positions observed by the *ISO* LWS. The 236 smaller circles (54'' diameter beams, within the dashed borders) mark positions observed by SPIFI on the AST/RO.

through a raster with a 130'' step size (a three-pixel overlap) to minimize flatfielding errors. The resulting map contains single-beam pointings at 236 distinct spatial positions with a  $\sim 54\%$  filling factor (where more extended spatial coverage was favored over denser spatial sampling). Two of SPIFI's 25 detectors were nonfunctional at the time of the Carina observations; as a result, seven of the 236 observed positions are lacking spectra (see Table 3). Pointing accuracy, refined by observing the limb of the Moon at 370  $\mu\text{m}$ , was  $\approx 1'$  (Oberst 2009).

Each spectrum covered seven resolution elements of width  $\Delta\lambda \approx 0.0483 \mu\text{m}$  (or 71  $\text{km s}^{-1}$  in terms of the relative Doppler velocity shift) slightly oversampled in 16 spectral bins of width  $\approx 0.0211 \mu\text{m}$  (31  $\text{km s}^{-1}$ ). The resolving power at 205  $\mu\text{m}$  was  $R = \lambda/\Delta\lambda \approx 4250 \pm 120$ . In each spectral bin, SPIFI measured the difference between the source and background sky using a three-position, 30'' azimuth throw, 2 Hz chop of the AST/RO's tertiary mirror. The total integration time for the Carina observations was 143 hr. Because SPIFI was spatially multiplexed by a factor of 25, this corresponds to an effective average integration time of  $\sim 15$  hr at each of the 236 distinct single-beam pointings, or  $\sim 1$  hr per spectral bin.

Wavelength calibration was achieved by measuring the  $\text{CD}_3\text{OH}$  205.4229  $\mu\text{m}$  laser line, which was used as the local oscillator for the Terahertz REceiver with NbN HEB Device (TREND; Yngvesson et al. 2004), also deployed on AST/RO in 2005. In terms of relative Doppler velocity shifts, the calibration uncertainty is estimated to be  $\pm \sim 2.7 \text{ km s}^{-1}$  (Oberst 2009). However, a comparison of the centroids of SPIFI's 205  $\mu\text{m}$  lines with previous radio recombination line observations of the Carina Nebula suggests an additional velocity offset in the SPIFI

data of  $\sim -7.5 \text{ km s}^{-1}$  (a blueshift of  $\sim 10\%$  of an SPIFI resolution element, see Section 4.5). This is likely due to calibration against an imperfectly collimated laser (but observation of perfectly collimated astrophysical lines), since rays passing through a Fabry-Perot off-axis see shorter resonant wavelengths than those along the optical axis.

Intensity calibration was achieved by measuring the gain ( $\text{mV K}^{-1}$ ) of hot and cold loads placed in the  $f$ -cone of the receiver and correcting by the efficiency of the AST/RO at 205  $\mu\text{m}$  (51%; A. A. Stark 2004, private communication) and the measured transparency of the sky at the time of the observations. The final absolute calibration uncertainty in intensity is estimated to be  $\pm 26\%$  (Oberst 2009).

SPIFI's sensitivity, as calibrated by SPIFI's chopper wheel over an hour-long integration, corresponded to a noise-equivalent power (NEP) of  $\sim 2.5 \times 10^{-15} \text{ W Hz}^{-1/2}$  (referred to the front end of the Dewar). This is within a factor of  $\sim 1.4$  of the fundamental limits imposed by the photon shot noise associated with the large thermal background from the (nearly opaque) sky at 205  $\mu\text{m}$  (Oberst 2009). This NEP is also a factor of  $\sim 10$  better than the best NEPs achieved by direct-detection spectrometers using photoconductor detectors (see Colgan et al. 1993). SPIFI's equivalent double side-band (DSB) receiver temperature ( $T_{\text{rec}}(\text{DSB}) \sim 150 \text{ K}$ ) is a factor of  $\sim 7$  better than the best temperatures achieved by heterodyne receivers near 200  $\mu\text{m}$  (Yngvesson et al. 2004).

These observations constitute the first published ground-based detection of the  $[\text{N II}]$  205  $\mu\text{m}$  line (Oberst et al. 2006) and the third detection overall since those collected by the *Cosmic Background Explorer* (COBE) Far Infrared Absolute

Spectrophotometer (FIRAS; Wright et al. 1991) and the *Kuiper Airborne Observatory* (KAO; Colgan et al. 1993) in the early 1990s.

## 2.2. ISO Observations

The Long Wavelength Spectrometer (LWS; Clegg et al. 1996) aboard the *Infrared Satellite Observatory* (ISO; Kessler et al. 1996) was used to obtain full bandwidth (43–197  $\mu\text{m}$ ) spectra of the Carina Nebula over four days—1996 July 23 and 24 and August 1 and 4—as part of a guaranteed time observation (GTO) by T. Onaka. Within the LWS band, fine-structure lines of [O I] 63  $\mu\text{m}$ , [N II] 122  $\mu\text{m}$ , [O I] 146  $\mu\text{m}$ , and [C II] 158  $\mu\text{m}$  (among others) were detected (Table 1), as previously reported by Mizutani et al. (2002, 2004).

These spectra were taken at 100 spatial positions within a  $\sim 40' \times 20'$  area centered at  $(l, b) = (287^\circ.4, -0^\circ.6)$  and containing the Car I and Car II regions (Figure 2). The ISO beam had an average FWHM of  $79''.3$  over the LWS band (Gry et al. 2003) and the pointings were spaced by  $180''$ , resulting in a  $\sim 16\%$  map filling factor (with more extended spatial coverage favored over denser spatial sampling).

The grating was scanned in the AOT LWS01 mode (or “fast” mode), sampling every  $1/4$  of a spectral resolution element, where the spectral resolution element was  $\Delta\lambda \approx 0.283 \mu\text{m}$  in the second grating order (detectors SW1–SW5, covering 43–93  $\mu\text{m}$ ) and  $\Delta\lambda \approx 0.584 \mu\text{m}$  in the first grating order (detectors LW 1–LW 5, covering 84–197  $\mu\text{m}$ ; Gry et al. 2003). The resulting resolving powers for the detected species range from  $R \approx 223$  to 270 (Table 1). The effective integration time was 0.45 s per spectral bin,  $\sim 13.2$  minute per raster position, and  $\sim 22$  hr for the entire (100 raster positions) map.

The LWS data were run through the standard ISO Off-Line Processing version 11.1 (OLP v11.1) pipeline (see Swinyard et al. 1998 and Gry et al. 2003 for full details of LWS calibration) and were further processed with the LWS L01 pipeline to produce “highly processed data products” (HPDP; Lloyd et al. 2003). The OLP pipeline automatically corrects for diffraction losses from on-axis point sources. These losses do not occur for extended sources such as Carina, resulting in a flux overestimation. Thus, extended source correction factors (Salama 2000; Gry et al. 2003) were applied. Finally, the present authors manually removed (rare) remaining glitches.

The final LWS absolute calibration uncertainty in flux is estimated to be  $\sim 20\%$  (Oberst 2009), wavelength calibration was measured to have an accuracy better than  $1/4$  resolution element (0.07  $\mu\text{m}$  for SW detectors and 0.15  $\mu\text{m}$  for LW detectors; Gry et al. 2003), and the pointing accuracy of the ISO at the time of the Carina observations was  $< 2''$  (Kessler et al. 2003).

## 3. RESULTS

### 3.1. SPIFI Results

A Markov chain Monte Carlo (MCMC)  $\chi^2$  algorithm was used to fit linear baselines and Lorentzian profiles (SPIFI’s Fabry-Perot profile is Lorentzian) to the 205  $\mu\text{m}$  [N II] lines in the spectra at each of the 236 positions in the Carina Nebula observed by SPIFI (Oberst 2009). After rejecting fits with signal-to-noise ratios (S/Ns)  $\lesssim 3$ , ionized nitrogen emission was detected (i.e., lines with fits of  $S/N \gtrsim 3$  were found) in over 40% of the positions mapped by SPIFI, with an average S/N at the detected positions of  $\sim 5$ .

Sample spectra and fits are shown in Figure 3, and a full list of the line intensities derived from fits to SPIFI’s spectra is provided in Table 3. The conversion between the main beam brightness temperature ( $T_{\text{MB}}$ ) and velocity ( $v_{\text{LSR}}$ ) values of the spectra in Figure 3 and the intensity ( $I$ ) values of Table 3 is

$$I = \frac{2k_{\text{B}}}{\lambda^3} \left( \frac{\pi}{2} T_{\text{MB}} \Delta v_{\text{LSR}} \right), \quad (1)$$

where  $k_{\text{B}}$  is Boltzmann’s constant, and  $T_{\text{MB}}$  and  $\Delta v_{\text{LSR}}$  are the height and FWHM of the fit to a spectral line, respectively.

Statistical ( $1\sigma$ ) noise values are also listed in Table 3, but do not include the absolute calibration uncertainty of  $\sim 26\%$ . At positions with intensities below the  $S/N \sim 3$  cutoff, theoretical upper limits to intensity have been calculated by taking the product of the noise and the width of a spectral resolution element ( $71 \text{ km s}^{-1}$ ).

The 205  $\mu\text{m}$  [N II] line intensities are plotted as a contour map in Figure 4. Because the SPIFI raster was spatially undersampled, intensities between observed positions were interpolated by averaging the intensities from surrounding observed positions weighted by both their noise and beam profiles. The final map was convolved with a two-dimensional (2D) Gaussian filter corresponding to the  $54''$  instrument beam size to smooth ersatz features with size scales smaller than the beam size. The interpolation and smoothing have somewhat attenuated the maxima of the map (theoretically, a  $\sim 20\%$  attenuation is expected from the convolution of two identical 2D Gaussians). Thus, while the maps are utilized for studying the morphology of the region, the original intensity values (Table 3) are used for any quantitative calculations.

### 3.2. ISO Results

The ISO spectra were fit in the same manner as the SPIFI spectra except that Gaussian profiles were used in order to match the LWS profile. Lines of 63  $\mu\text{m}$  [O I], 122  $\mu\text{m}$  [N II], 146  $\mu\text{m}$  [O I], and 158  $\mu\text{m}$  [C II] were detected at all 100 positions observed by ISO, with average S/Ns of 40, 21, 8.4, and 71 for the four species, respectively. None of the fits fell below our  $S/N = 3$  cutoff.

Sample spectra are shown in Figure 10 and intensities derived from the fits are reported in Table 4. The table lists statistical ( $1\sigma$ ) errors for each measurement, but does not include the absolute calibration uncertainty of  $\sim 20\%$ . The conversion between the specific flux ( $F_{\nu}$ ) and wavelength ( $\lambda$ ) values of the spectra in Figure 10 and the intensity ( $I$ ) values in Table 4 is

$$I = \sqrt{\frac{\pi}{4 \ln 2}} F_{\nu} \Delta\lambda, \quad (2)$$

where  $F_{\nu}$  and  $\Delta\lambda$  are the height and FWHM of the fit to the spectral line, respectively.

Contour maps for each of the four spectral species are shown in Figures 6–9 (the gray-scale contours). These maps were created in the same manner as described above for the SPIFI contour map. The dimensions of the axes in these maps match those of Figure 1, with areas outside of the ISO raster (outlined by the solid line) grayed-out.

We find the 158  $\mu\text{m}$  [C II] intensities to be consistently  $\sim 35\%$  higher and the 122  $\mu\text{m}$  [N II] intensities to be consistently  $\sim 25\%$  lower than those reported by Mizutani et al. (2002, 2004) for the same raw data sets, while the 63  $\mu\text{m}$  [O I] intensities were more or less the same. More significantly, we find good

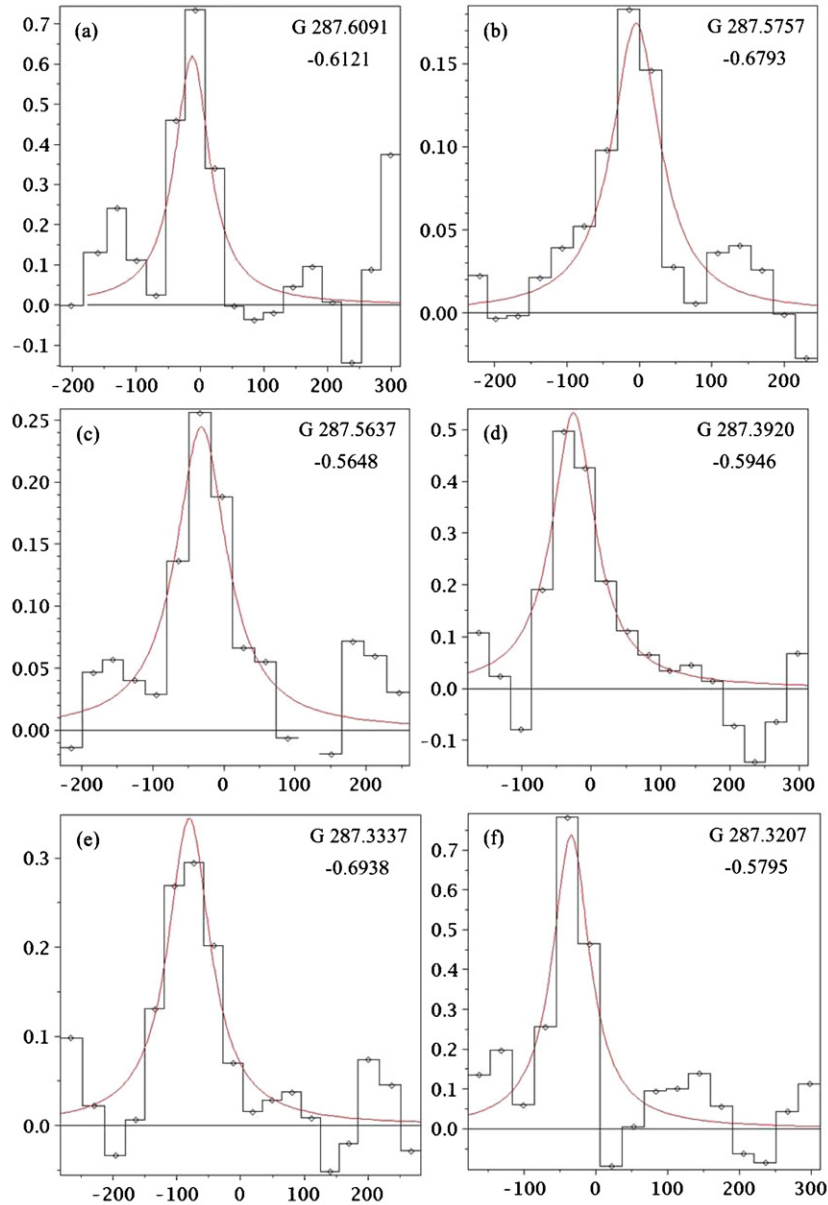


**Figure 3.** Select detections of the  $205\ \mu\text{m}$  [N II]. Spectral line spectra in the vicinity of Car II are shown in panels (a), (b), and (c) (SPIFI raster positions 169, 174, and 198, respectively), and spectra in the vicinity of Car I are shown in panels (d), (e), and (f) (SPIFI raster positions 29, 45, and 73, respectively). (Galactic coordinates are also provided in the upper right of each panel.) The (black) data points and bars mark the processed data, and the (red) smooth curves are the least  $\chi^2$  Lorentzian fits. The  $x$ -axes give the source velocity relative to the local standard of rest,  $v_{\text{LSR}}$ , in units of  $\text{km s}^{-1}$ , and the  $y$ -axes give the main beam brightness temperature,  $T_{\text{MB}}$ , in units of K. The data have been smoothed with a Hann window.

(A color version of this figure is available in the online journal.)

detections of  $146\ \mu\text{m}$  [O I] at all of the 100 raster positions observed by *ISO*, with an average S/N of  $\sim 8.4$  over the entire map. Mizutani et al., on the other hand, reported  $146\ \mu\text{m}$  [O I] detections at only 10 of the 100 positions, with marginal S/Ns of  $\sim 2.5$ – $3$ . While slight differences are to be expected between the reductions of Mizutani et al. and the current work due to improvements in the *ISO* LWS calibration (from OLP version 8–11), this cannot account for a tripling of the S/N of the  $146\ \mu\text{m}$  data. Unfortunately, the details of the Mizutani et al. fits are no longer available (T. Onaka 2007, private communication). Based on our analysis, they appear to suffer from systematic scaling errors in intensity. We contend that the present fits are a more robust and accurate representation of the raw data.

## 4. ANALYSIS AND DISCUSSION

### 4.1. Morphology

#### 4.1.1. Ionized Component

In the region mapped, the  $205\ \mu\text{m}$  [N II] emission observed by SPIFI (Figure 4) has two main peaks: a primary peak of intensity  $51.7 \times 10^{-8}\ \text{W m}^{-2}\ \text{sr}^{-1}$  at  $(l, b) = (287.3843, -0.6301)$  and a secondary peak of intensity  $27.4 \times 10^{-8}\ \text{W m}^{-2}\ \text{sr}^{-1}$  at  $(287.5519, -0.6182)$  (raster positions 27 and 195 in Table 3, respectively). The peaks are separated by  $10''.08$  (6.74 pc).

To compare morphologies, we overlay the  $205\ \mu\text{m}$  [N II] map with the  $122\ \mu\text{m}$  [N II] and  $57\ \mu\text{m}$  [N III] line emission observed by *ISO* (Figures 7 and 5, respectively), and the 843 MHz radio



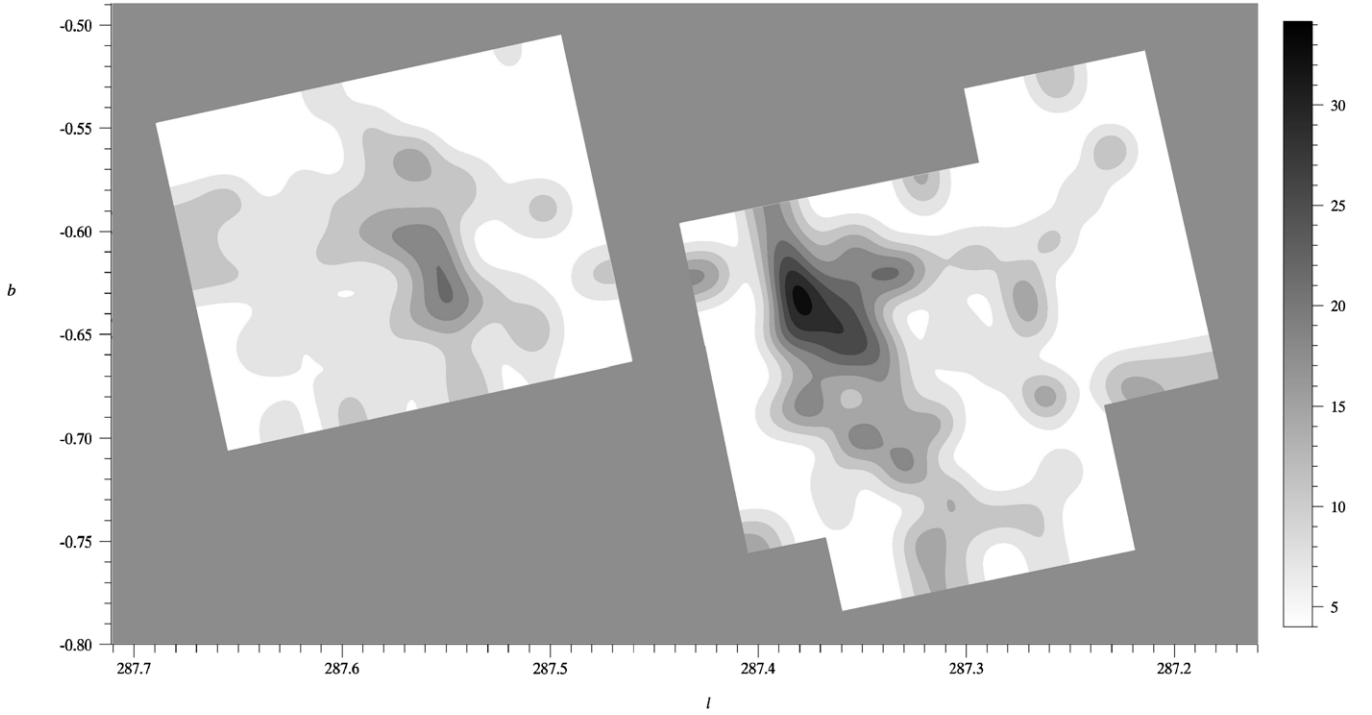


**Figure 4.** SPIFI  $205\ \mu\text{m}$  [N II] map of the Carina Nebula.  $205\ \mu\text{m}$  [N II] line emission in the Carina Nebula, observed by SPIFI from the AST/RO. The inverted gray-scale bar measures intensity in units of  $10^{-8}\ \text{W m}^{-2}\ \text{sr}^{-1}$ . Contours are shown every  $1\sigma$  starting at the  $2\sigma$  level, where  $\sigma = 3.8 \times 10^{-8}\ \text{W m}^{-2}\ \text{sr}^{-1}$  is the average intensity error over the map. The map has been resampled and smoothed with a Gaussian filter of  $\text{FWHM} = 54''$ , matching the SPIFI beam. Smoothing has attenuated the maxima; the original unsmoothed data are listed in Table 3.

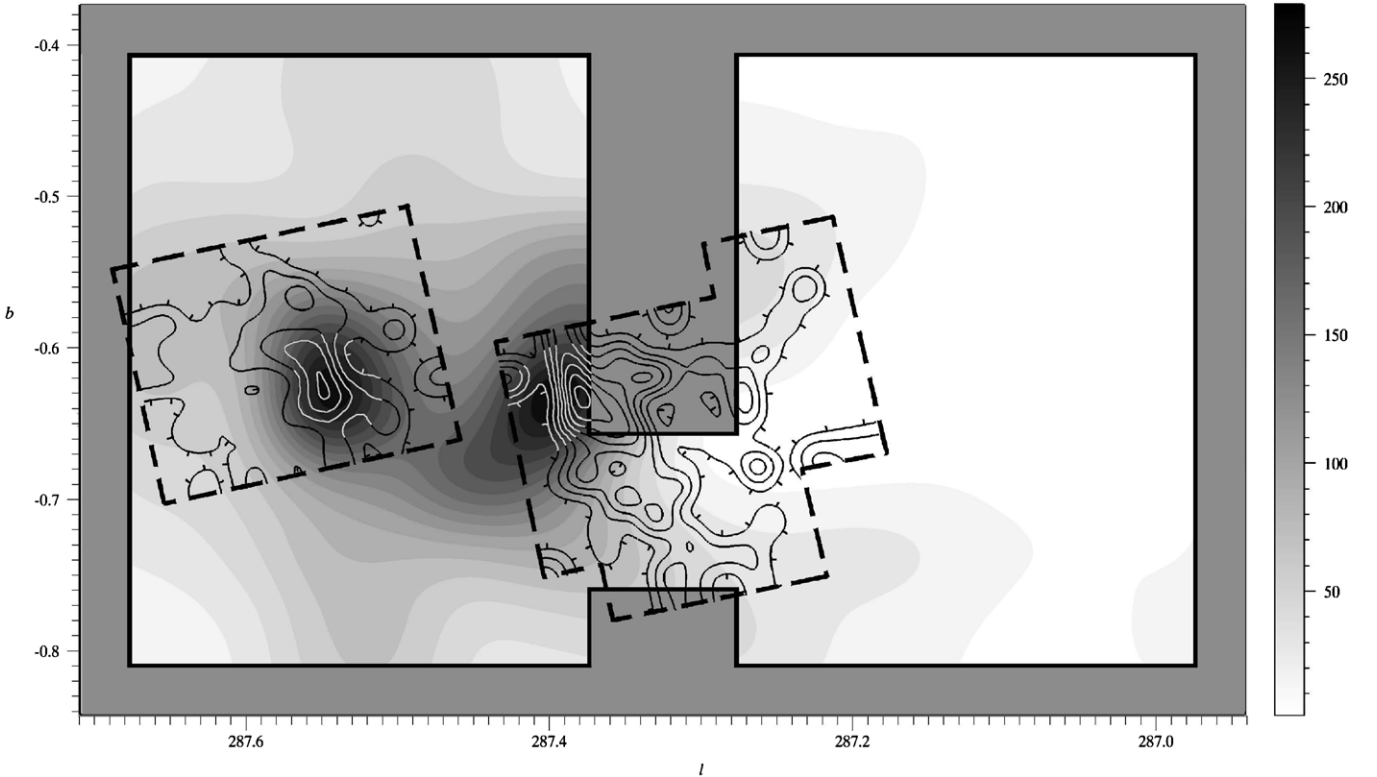


**Figure 5.**  $205\ \mu\text{m}$  [N II] and  $57\ \mu\text{m}$  [N III] overlay. SPIFI [N II]  $205\ \mu\text{m}$  contours (lines; corresponding to Figure 4) overlaid on ISO  $57\ \mu\text{m}$  [N III] contours (gray scale). Details of the  $57\ \mu\text{m}$  [N III] map: the inverted gray-scale bar measures intensity in units of  $10^{-8}\ \text{W m}^{-2}\ \text{sr}^{-1}$ . Contours are shown every  $5\sigma$ , where  $\sigma = 3.1 \times 10^{-8}\ \text{W m}^{-2}\ \text{sr}^{-1}$  is the average intensity error over the map. The map has been resampled and smoothed with a Gaussian filter of  $\text{FWHM} = 84''5$ , matching the LWS beam. Smoothing has attenuated the maxima; the original unsmoothed data are listed in Table 4.

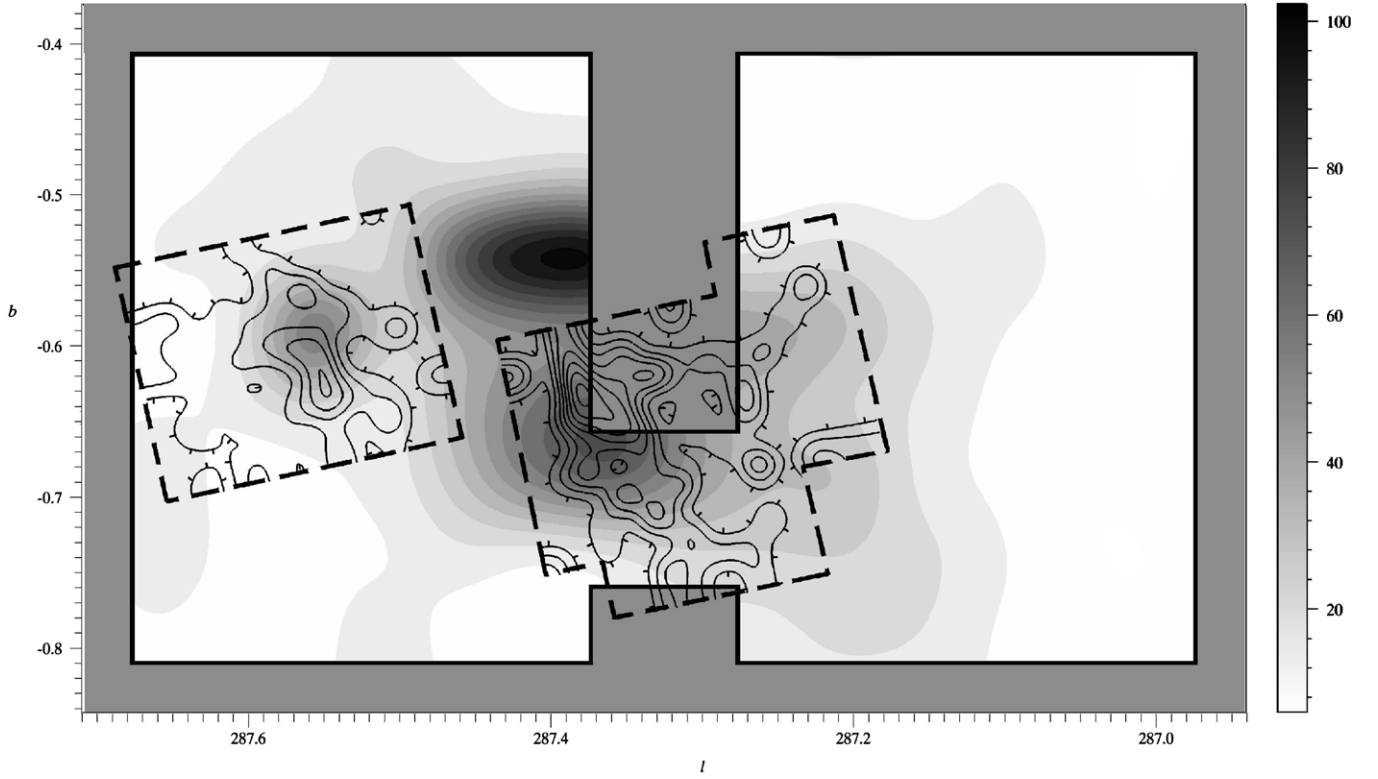


**Figure 6.** 205  $\mu\text{m}$  [N II] and 63  $\mu\text{m}$  [O I] overlay. SPIFI [N II] 205  $\mu\text{m}$  contours (lines; corresponding to Figure 4) overlaid on *ISO* 63  $\mu\text{m}$  [O I] contours (gray scale). Details of the 63  $\mu\text{m}$  [O I] map: the inverted gray-scale bar measures intensity in units of  $10^{-8} \text{ W m}^{-2} \text{ sr}^{-1}$ . Contours are shown every  $10\sigma$ , where  $\sigma = 0.6 \times 10^{-8} \text{ W m}^{-2} \text{ sr}^{-1}$  is the average intensity error over the map. The map has been resampled and smoothed with a Gaussian filter of  $\text{FWHM} = 87''.2$ , matching the LWS beam. Smoothing has attenuated the maxima; the original unsmoothed data are listed in Table 4.

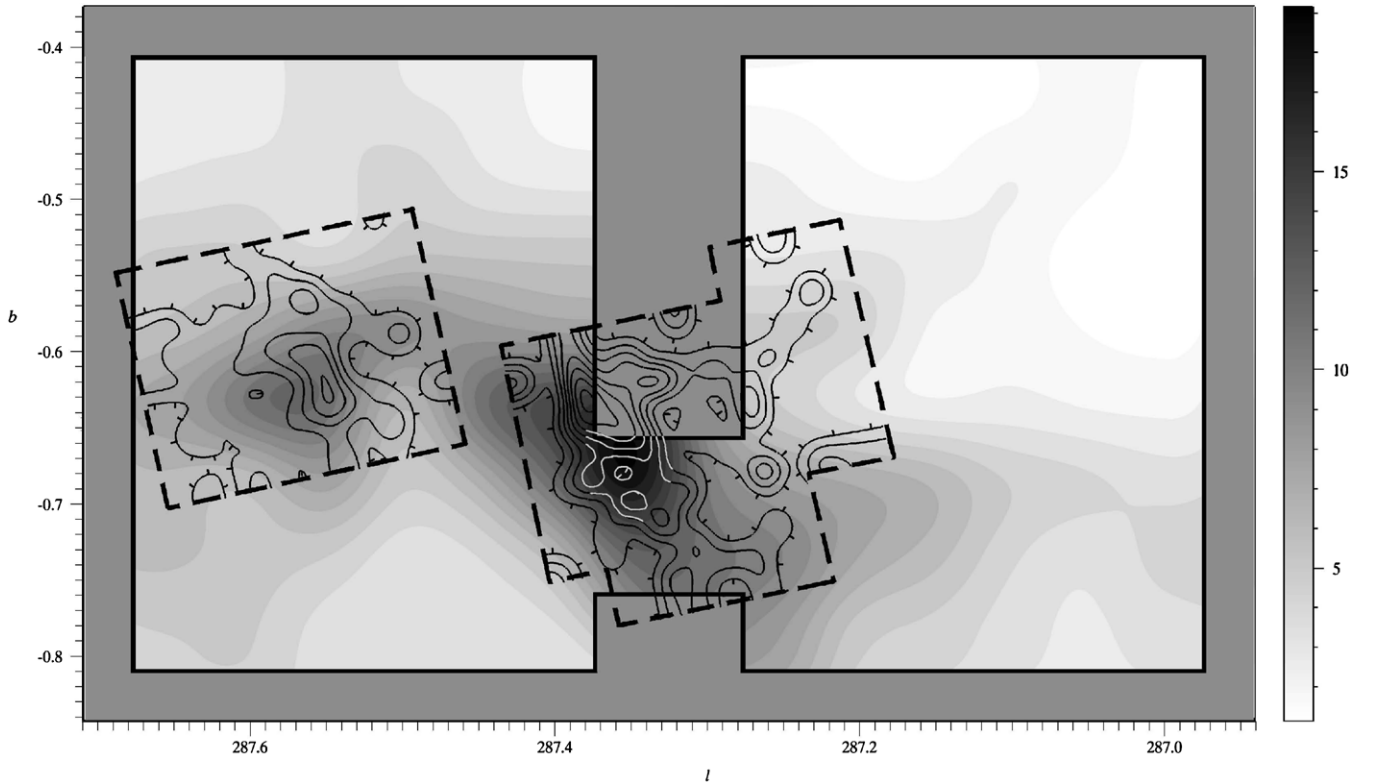


**Figure 7.** 205 and 122  $\mu\text{m}$  [N II] overlay. SPIFI [N II] 205  $\mu\text{m}$  contours (lines; corresponding to Figure 4) overlaid on *ISO* 122  $\mu\text{m}$  [N II] contours (gray scale). Details of the 122  $\mu\text{m}$  [N II] map: the inverted gray-scale bar measures intensity in units of  $10^{-8} \text{ W m}^{-2} \text{ sr}^{-1}$ . Contours are shown every  $3\sigma$ , where  $\sigma = 0.3 \times 10^{-8} \text{ W m}^{-2} \text{ sr}^{-1}$  is the average intensity error over the map. The map has been resampled and smoothed with a Gaussian filter of  $\text{FWHM} = 78''.2$ , matching the LWS beam. Smoothing has attenuated the maxima; the original unsmoothed data are listed in Table 4.

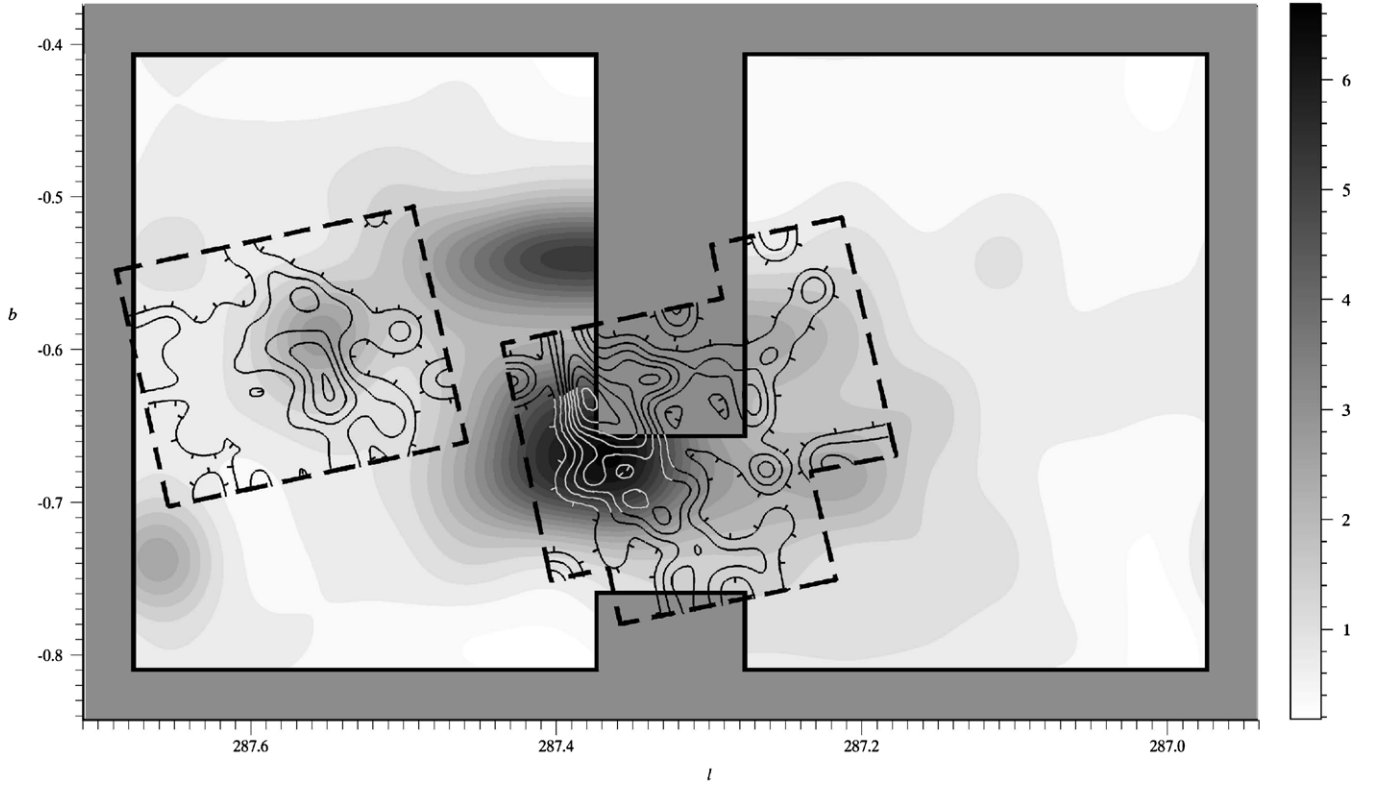


**Figure 8.** 205  $\mu\text{m}$  [N II] and 146  $\mu\text{m}$  [O I] overlay. SPIFI [N II] 205  $\mu\text{m}$  contours (lines; corresponding to Figure 4) overlaid on *ISO* 146  $\mu\text{m}$  [O I] contours (gray scale). Details of the 146  $\mu\text{m}$  [O I] map: the inverted gray-scale bar measures intensity in units of  $10^{-8} \text{ W m}^{-2} \text{ sr}^{-1}$ . Contours are shown every  $3\sigma$ , where  $\sigma = 0.1 \times 10^{-8} \text{ W m}^{-2} \text{ sr}^{-1}$  is the average intensity error over the map. The map has been resampled and smoothed with a Gaussian filter of  $\text{FWHM} = 70''.0$ , matching the LWS beam. Smoothing has attenuated the maxima; the original unsmoothed data are listed in Table 4.

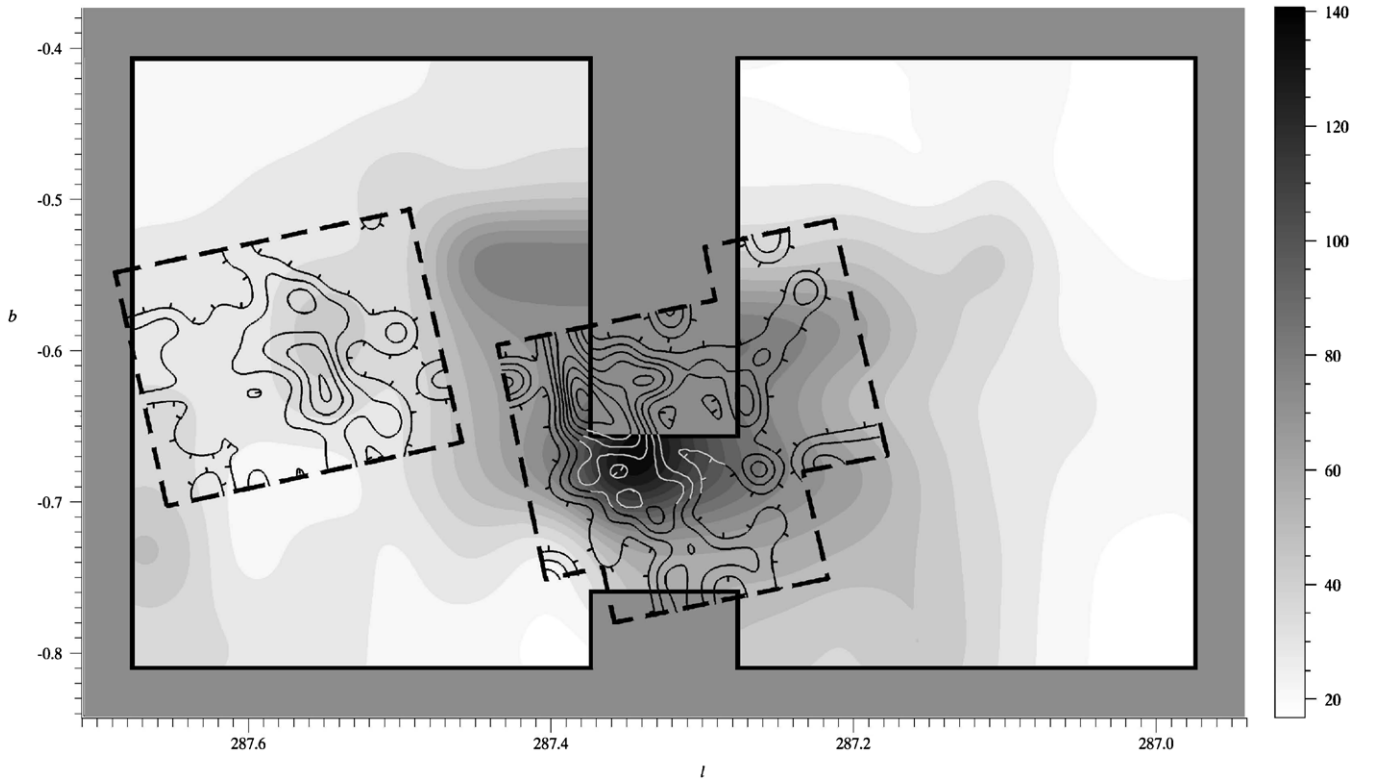


**Figure 9.** 205  $\mu\text{m}$  [N II] and 158  $\mu\text{m}$  [C II] overlay. SPIFI [N II] 205  $\mu\text{m}$  contours (lines; corresponding to Figure 4) overlaid on *ISO* 158  $\mu\text{m}$  [C II] contours (gray scale). Details of the 158  $\mu\text{m}$  [C II] map: the inverted gray-scale bar measures intensity in units of  $10^{-8} \text{ W m}^{-2} \text{ sr}^{-1}$ . Contours are shown every  $10\sigma$ , where  $\sigma = 0.7 \times 10^{-8} \text{ W m}^{-2} \text{ sr}^{-1}$  is the average intensity error over the map. The map has been resampled and smoothed with a Gaussian filter of  $\text{FWHM} = 70''.1$ , matching the LWS beam. Smoothing has attenuated the maxima; the original unsmoothed data are listed in Table 4.



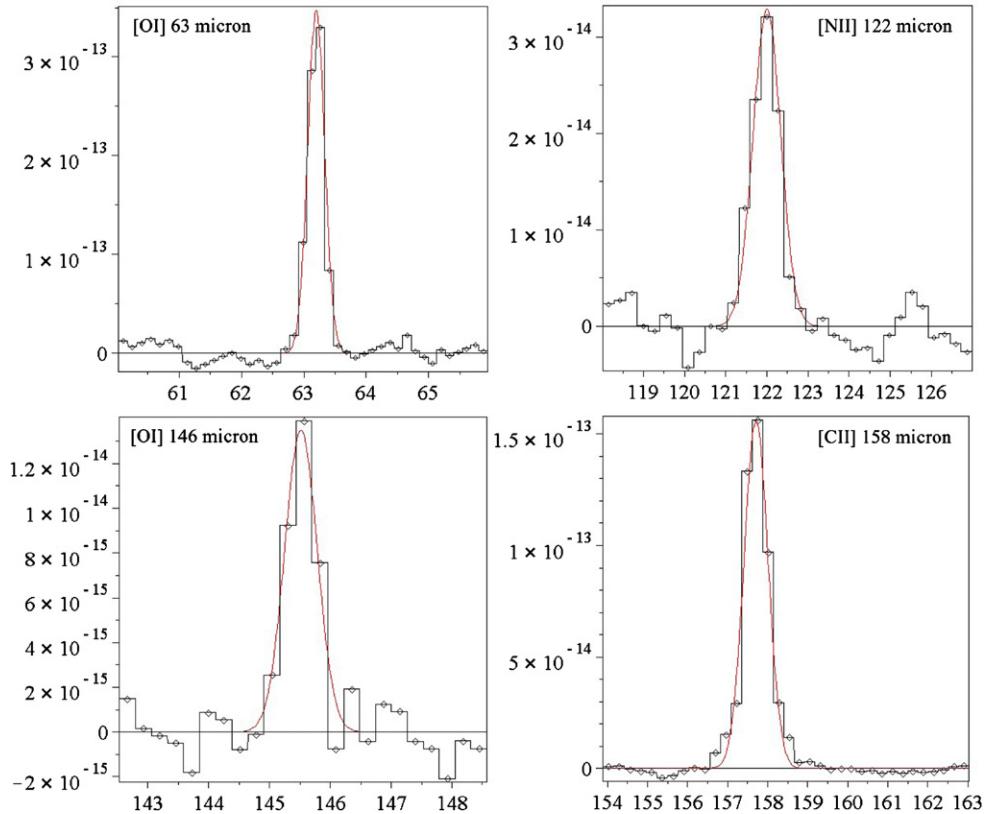


**Figure 10.** Select detections of spectral lines in the Carina Nebula by the *ISO* LWS. Detections of the [OI] 63  $\mu\text{m}$  (top left), [N II] 122  $\mu\text{m}$  (top right), [OI] 146  $\mu\text{m}$  (bottom left), and [C II] 158  $\mu\text{m}$  (bottom right) spectral lines in the Carina Nebula by the *ISO* LWS. All four spectra were taken at  $(l, b) = (287.405, 0.637)$  (the “Car 4:19” raster position in Table 4), which lies between the Car I peak and Tr 14. The  $x$ -axes give the wavelength,  $\lambda$ , in units of  $\mu\text{m}$ , and the  $y$ -axes give the specific flux,  $F_\nu$ , in units of  $\text{W m}^{-2} \mu\text{m}^{-1}$ . The (black) data points and bars mark the processed data, the (red) smooth lines are the least  $\chi^2$  Gaussian fits.

(A color version of this figure is available in the online journal.)

continuum emission observed by the Molonglo Observatory Synthesis Telescope (MOST; Whiteoak 1994; Figure 12). (The [N III] map, generated directly from the data of Mizutani et al. 2002, may suffer the intensity scaling error discussed in Section 3.2; it is considered here for morphology only.)

The 205  $\mu\text{m}$  [N II] peaks line up fairly closely with the 843 MHz radio peaks: offset just  $51''$  (0.57 pc) eastward of Car I and  $41''$  (0.46 pc) southwest of Car II (see Figures 11 and 12). Given that the beam sizes of both maps and the SPIFI pointing accuracy were  $\sim 1'$ , and that the SPIFI map had a  $\sim 50\%$  filling factor, the two maps are in very good agreement. Nitrogen has an ionization potential of 14.53 eV, and can arise only in ionized regions. Radio emission can also arise in ionized regions due to thermal free-free transitions. From the agreement of the maps, it is clear that both the [N II] lines and radio continuum emission originate in the ionized gas component of the Carina Nebula.

The closest morphological match to the SPIFI 205  $\mu\text{m}$  [N II] map among the *ISO* data is the 122  $\mu\text{m}$  [N II] map, as should be expected (Figure 7). Although the *ISO* beam is larger and its spatial sampling coarser (Section 2), the strong correlation of the two [N II] maps shows that the two instruments are in good agreement.

We note two features of the ionized component evident in these maps.

1. The lower ionization [N II] gas has a Car I peak farther to the southwest and is also extended over a greater area of the sky to the south and west of Car I than is the more highly ionized [N III] (compare Figures 7 and 5). The respective Car I peaks of 122  $\mu\text{m}$  [N II] and 57  $\mu\text{m}$  [N III] occur at

$(l, b) = (287.355, -0.686)$  (*ISO* raster position “Car 6:7” in Table 4) and  $(l, b) = (287.405, -0.637)$  (“Car 4:19”). This is consistent with the predominant view that the Car I emission peak is powered externally by the members of Tr 14 to the northeast (e.g., Retallack 1983; Whiteoak 1994; Mizutani et al. 2002; Brooks et al. 2003; Tapia et al. 2006) and that Car I sits just outside the edge of a GMC extending to the south and west (see Figure 11). (Embedded sources cannot be ruled out, however, Tapia et al. 2003 have detected an embedded stellar population in Car I which includes at least one O9/B0 star.) In other words, the more highly ionized gas exists primarily near the ionizing source, where the parent molecular cloud has been mostly ionized or swept away. The lower ionization gas, on the other hand, extends further from the ionizing source, and is either projected along the same line of sight as the molecular component or appears intermixed with it at the angular resolution of our beam.

2. For all of the observed species discussed here which trace the ionized component ([N II], [N III], and the radio continuum), emission is extended over a fairly large area of the sky. In Section 4.2, we derive a density of  $n_e \sim 28 \text{ cm}^{-3}$  from the [N II] emission, supporting the suggestion of Mizutani et al. (2002) that an extended low-density (ELD) H II region spans 30 pc or more across the nebula.

#### 4.1.2. Neutral Component

The 205  $\mu\text{m}$  [N II] emission contours observed by SPIFI (Figure 4) are overlaid on the 63  $\mu\text{m}$  [OI], 146  $\mu\text{m}$  [OI], and

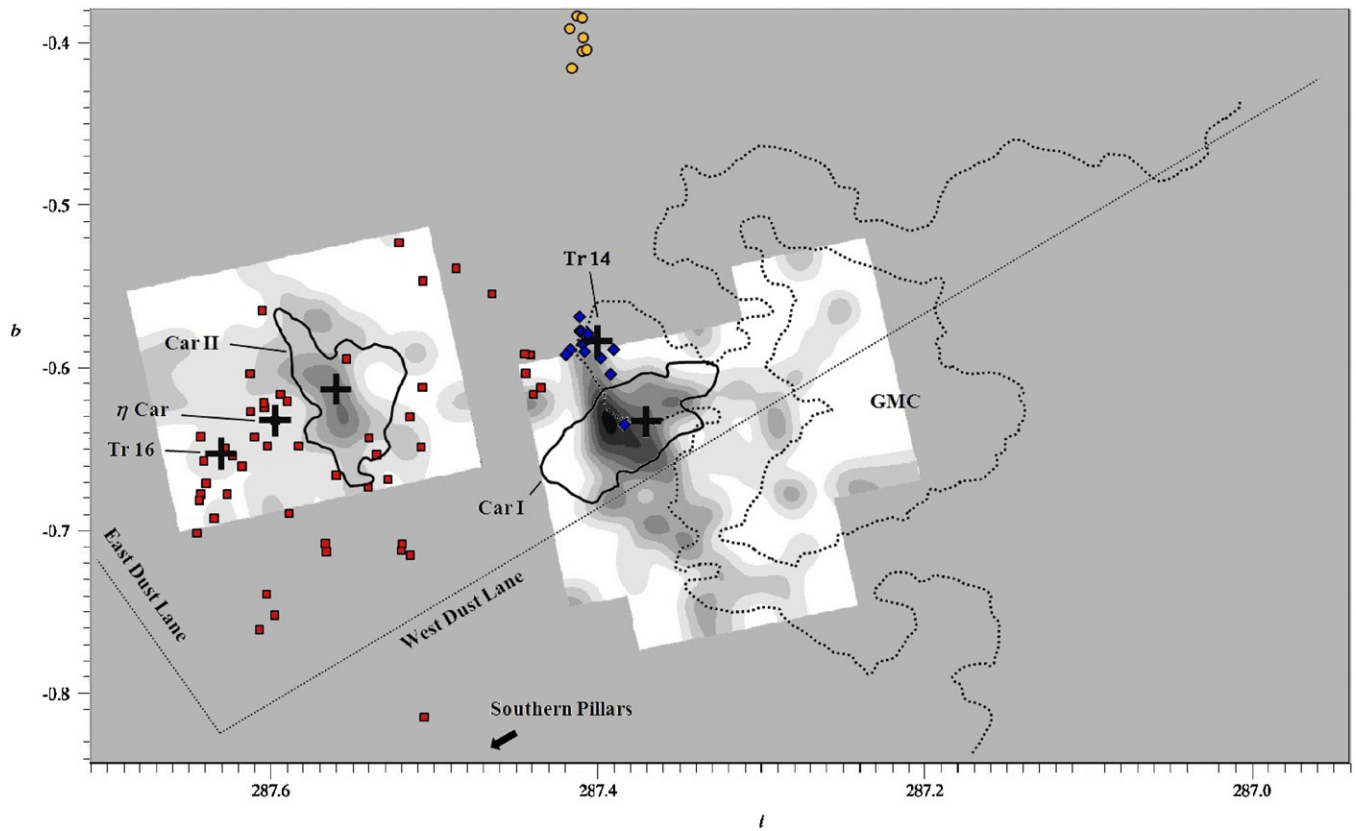


**Figure 11.** Morphological comparison of Carina sources and  $205\ \mu\text{m}$  [N II] emission. Major components of the Carina Nebula (Figure 1) are overlaid on SPIFI  $205\ \mu\text{m}$  [N II] contours (gray scale, from Figure 4).

(A color version of this figure is available in the online journal.)

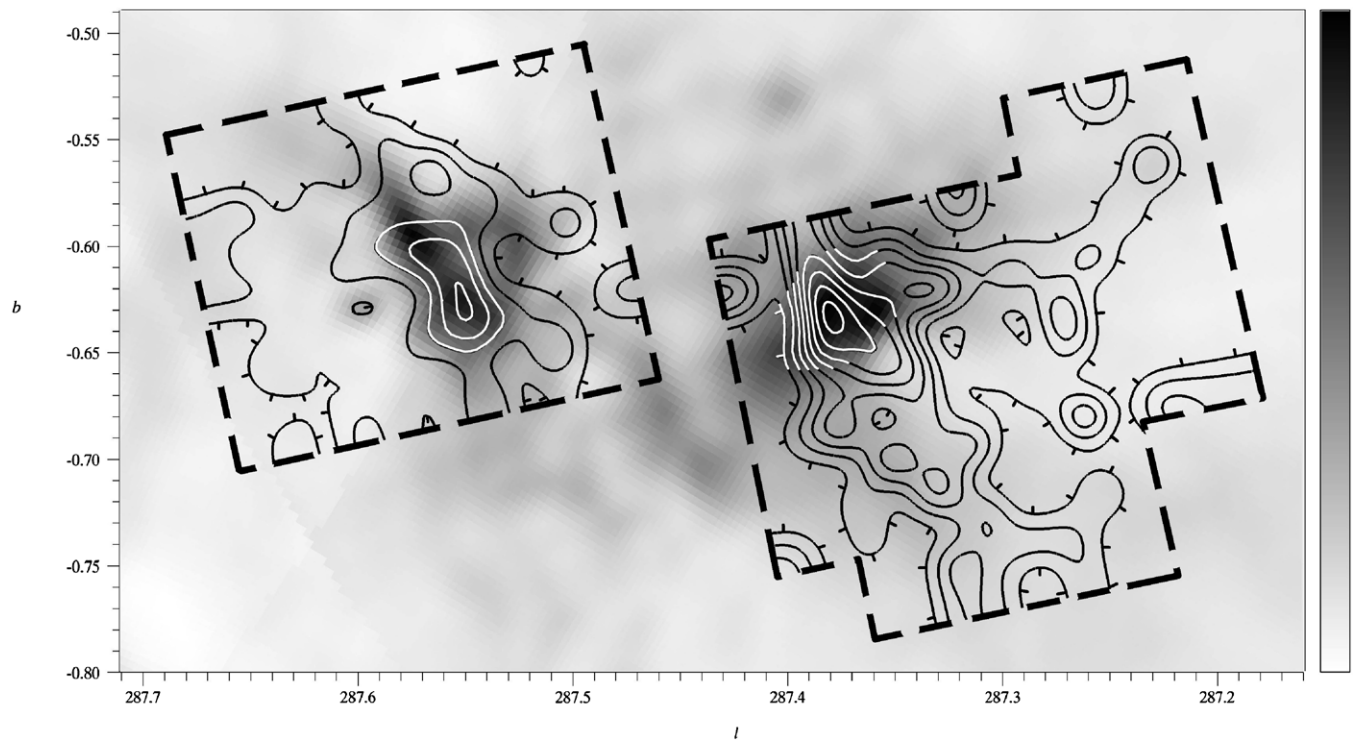


**Figure 12.**  $205\ \mu\text{m}$  [N II] and 843 MHz radio continuum overlay. SPIFI [N II]  $205\ \mu\text{m}$  contours (lines, from Figure 4) are overlaid on the MOST 843 MHz radio continuum map (gray scale). The 843 MHz gray-scale bar ranges linearly from 0 to  $2\ \text{Jy beam}^{-1}$ ; the beam size of the radio data was  $43'' \times 50''$  (R.A.  $\times$  decl.).

158  $\mu\text{m}$  [C II] emission observed by *ISO* in Figures 6, 8, and 9, respectively. Oxygen has an ionization potential of 13.62 eV, so [O I] arises entirely in the neutral interstellar medium (ISM). Carbon, on the other hand, has an ionization potential of 11.26 eV, so [C II] can arise from both the neutral and ionized phases of the ISM.

However, in our contour overlays, [C II] appears morphologically more akin to the neutral [O I] species than the ionized [N II] species. This is supported quantitatively by the analysis of Section 4.3 below, in which we find that  $\sim 63\%$  of the observed [C II] arises from the neutral medium. We conclude that [C II] predominately traces the neutral component in the Carina Nebula.

We note two features of the neutral component evident in these maps.

1. In the Car I region, [O I] and [C II] both peak slightly ( $\sim 1$  pc) to the southwest of the 205  $\mu\text{m}$  [N II] peak, at  $(l, b) = (287.355, -0.686)$  (raster position “Car 6:7” in Table 4). Thus, starting from Tr 14 and heading southwest in the plane of the sky, one encounters first the 57  $\mu\text{m}$  [N III] peak (tracing the highly ionized component), then the 205  $\mu\text{m}$  [N II] peak (tracing the lower ionization component), then the 63  $\mu\text{m}$  [O I], 146  $\mu\text{m}$  [O I], and 158  $\mu\text{m}$  [C II] peaks (all of which trace the neutral component), and then finally the GMC peak (tracing the molecular component). (The 122  $\mu\text{m}$  [N II] peak is near those of the neutral species—although this could be an artifact of coarse spatial sampling.) Observations of neutral 609  $\mu\text{m}$  [CI] line emission (Zhang et al. 2001) and several polycyclic aromatic hydrocarbon (PAH) features (Rathborne et al. 2002, Kramer et al. 2008)—all of which trace the photodissociated neutral gas—also show peaks near those of our [O I] and [C II] maps.

This again supports the view of Tr 14 as the external ionizing source for Car I (cf. Section 4.1.1), with the neutral line emission ([O I] and [C II]) arising from the photodissociated surface of the nearby GMC. The peak of the PDR emission occurs roughly at  $(l, b) \sim (287.355, -0.686)$ , corresponding to the northeastern surface of the GMC viewed edge-on along our line of sight—sandwiched between the ionized region near Tr 14 to the northeast and the greater GMC to the southwest. As was the case for the ionized gas, the tracers of photodissociated neutral gas extend well (several parsecs) to the south and west of Car I, indicating either that the FUV flux of Tr 14 penetrates deep into the GMC, or that a large fraction of the GMC surface (perpendicular to our line of sight) has undergone some photodissociation.

2. The neutral gas peak near Car II is relatively much weaker compared to Car I than was the case for the ionized gas. This is consistent with Tr 16 being an older (age of  $\sim 3$  Myr; Smith 2006a) more evolved cluster which has ionized or swept away most of its parental cloud. On the contrary, the younger (age of  $\sim 1.5$  Myr; Smith 2006a) Tr 14 cluster is situated much closer ( $\sim 2$  pc) from the northeastern edge of the remaining GMC, which also wraps behind Tr 14 along the line of sight. As evidenced by the PDR emission in its vicinity, Tr 14 is still actively eroding its parental cloud.

We conclude our study of the neutral morphology of Carina by pointing out the strong neutral peak (most evident in the 63  $\mu\text{m}$  [O I] map) at  $(l, b) \sim (287.405, -0.536)$  (raster position “Car 2:7” in Table 4) near the Tr 14 cluster. Since the 63  $\mu\text{m}$  [O I]

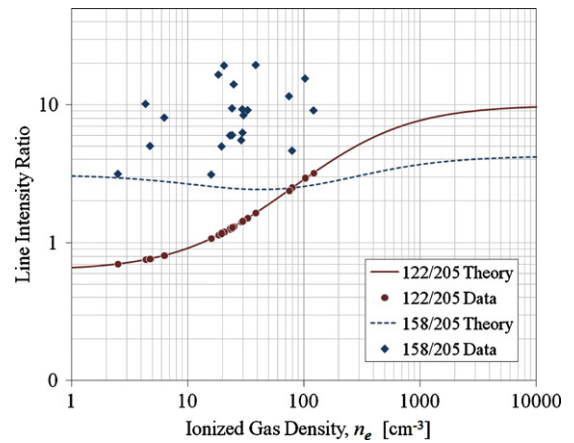


**Figure 13.** [C II] and [N II] line intensity ratios in the Carina Nebula. Theoretical and measured values of observed line intensity ratios are plotted vs. the electron density of the ionized medium. The 122/205  $\mu\text{m}$  [N II] line ratio theoretical curve and data are shown by the (red) solid line and circles, respectively, and the 158  $\mu\text{m}$  [C II] to 205  $\mu\text{m}$  [N II] ratio theoretical curve and data are shown by the (blue) dashed line and diamonds, respectively. The 122/205  $\mu\text{m}$  data and theory coincide because the theoretical curve was used to derive the electron densities from the measured line ratios (see the text). Numerical values and errors for the plotted densities can be found in Table 5; error bars are omitted here for clarity. (A color version of this figure is available in the online journal.)

line can be enhanced in shocks, one might consider invoking shock excitation near Tr 14. However, the [O I]/[C II] line intensity ratio there is similar to other positions in the map, and the [C II] line is not enhanced by shocks. In terms of PDR parameters (see Section 4.4), this region is a peak not unlike other peaks in the neutral gas line maps. At low densities, the [N II] line intensities should scale as the emission measure ( $n_e^2 d$ ), as does the radio free-free emission flux. At Tr 14, there is no peak in the free-free emission, so the large [O I]/[N II] line intensity ratio there likely just reflects less ionized gas in this region. Slightly enhanced PAH emission is seen near this position in the observations of Rathborne et al. (2002) and Kramer et al. (2008). This is consistent with PDR activity, possibly on the surface of the northeasterly portion of the GMC that wraps behind Tr 14, relative to our line of sight (see Figure 11).

#### 4.2. The Density of the Ionized Medium

The ratio of the 122  $\mu\text{m}$  to 205  $\mu\text{m}$  [N II] line intensities (hereafter “122/205”) provides an excellent density probe of the diffuse weakly ionized gas in the ISM. Because it takes relatively low-energy photons (14.53 eV) to form  $\text{N}^+$ , these lines arise in the lower ionization “outskirts” of H II regions. Furthermore, the 122 and 205  $\mu\text{m}$  [N II] lines have critical densities of  $n_e \sim 293 \text{ cm}^{-3}$  and  $44 \text{ cm}^{-3}$  at  $T = 8000 \text{ K}$ , respectively, so that the 122/205 ratio is sensitive to gas densities of  $n_e \lesssim 300 \text{ cm}^{-3}$ . The theoretically expected curve of 122/205 as a function of electron density,  $n_e$ , is plotted in Figure 13 (solid line). The curve assumes electron-impact excitation and uses the collision strengths from Hudson & Bell (2004), scaled to an assumed electron temperature of 8000 K.

Because the *ISO* and SPIFI rasters are not spatially aligned (Figure 2), a direct division of the 122 and 205  $\mu\text{m}$  maps was not possible. However, 27 of the *ISO* beams are overlapped by one or more SPIFI beams. By interpolating the 205  $\mu\text{m}$  [N II] intensities at the centers of these *ISO* beams (averaged and weighted by the SPIFI beam profiles and noises), the 122/205 ratio could



be computed. Finally, to derive  $n_e$ , we matched our observed 122/205 ratios to the theoretical 122/205 curve (circles and solid line, respectively, in Figure 13). A full list of the 27 derived  $n_e$  values is provided in Table 5.

The average electron density (in the low-ionization gas) is found to be a modest  $n_e \sim 28 \text{ cm}^{-3}$ , with little spatial variation over the nebula ( $n_e \sim 0\text{--}100 \text{ cm}^{-3}$ ). This average is close to the value of  $n_e \sim 32 \text{ cm}^{-3}$  previously determined at the Car II peak (Oberst et al. 2006).

Using the intensity ratio of the higher ionization 52 and  $88 \mu\text{m}$  [O III] lines, Mizutani et al. (2002) found two distinct components to the electron density in the Carina Nebula: a high-density ( $n_e \sim 100\text{--}350 \text{ cm}^{-3}$ ) component at Car I and II and an extended low-density (ELD;  $n_e < 100 \text{ cm}^{-3}$ ) component detectable over the entire  $\sim 30 \text{ pc}$  mapped region. From the present analysis, it is thus clear that the ELD “halo” also contains gas of lower ionization states.

#### 4.3. The Fraction of $\text{C}^+$ from PDRs

$\text{C}^+$  has an ionization potential of 11.26 eV, and hence can arise from both PDRs and H II regions. Because the  $158 \mu\text{m}$  [C II] line is often the brightest FIR line, and is a dominant coolant for much of the ISM, determining the fraction of the observed [C II] line radiation that arises from the neutral and ionized gas components is critical to the study of star-forming regions. Our observations of the  $205 \mu\text{m}$  [N II] line provide a direct means to measure this abundance ratio: since the critical densities for electron-impact excitation of the  $158 \mu\text{m}$  [C II] and  $205 \mu\text{m}$  [N II] lines are very similar ( $40$  and  $44 \text{ cm}^{-3}$ , respectively), to a good approximation the 158/205 line intensity ratio is dependent only on the relative abundance of  $\text{C}^+$  and  $\text{N}^+$  in the ionized medium.

Using the collision rates for exciting the ground-state levels of  $\text{C}^+$  from Blum & Pradhan (1992), we plot the expected ratio of the two lines as a function of electron density in Figure 13 (dashed line). The temperature dependence is quite small, as the  $^2\text{P}_{3/2}$  level of  $\text{C}^+$  and the  $^3\text{P}_1$  level of  $\text{N}^+$  are only 91 and 70 K above ground, respectively—small compared with the temperature (8000 K) of an H II region. For the calculation, we take the gas-phase abundances of  $\text{C}/\text{H} = 1.4 \times 10^{-4}$  (Kaufman et al. 1999) and  $\text{N}/\text{H} = 7.8 \times 10^{-5}$  (Savage & Sembach 1996).

As was done for the 122/205 ratio (Section 4.2), we determine the 158/205 ratio at the 27 positions in the ISO raster which are partially overlapped by SPIFI beams by interpolating the SPIFI  $205 \mu\text{m}$  [N II] intensities there. The resulting data points are plotted in Figure 13 (diamonds), where the electron densities for these points are taken as those derived from the 122/205 ratios.

For each point, the ratio of the expected to measured value represents the fraction of  $\text{C}^+$  which arises from the ionized gas. The remaining fraction must arise from the PDRs. All of the data lie above the theoretical curve, indicating that some fraction of the  $\text{C}^+$  arises from the neutral medium at every position. Spatially, we find, rather unsurprisingly, that a higher percentage of  $\text{C}^+$  arises from PDRs in locations where there are PDRs—e.g., over the surface of the GMC (a contour map of the percentage of  $\text{C}^+$  arising from PDRs, which demonstrates this effect, can be found in Oberst 2009). A lower percentage of  $\text{C}^+$  arises from PDRs in locations where there are no PDRs—e.g., in the vicinity of Tr 14 and 16, where winds from stellar members have driven away most of the gas and dust.

On average over these 27 positions in the nebula, we find that 63% of the  $\text{C}^+$  comes from PDRs and 37% from the ionized

gas. This result agrees with previous studies which contend that the majority of the observed [C II] line emission from Galactic star-forming regions, the Galaxy as a whole, and from external galaxies arises in warm dense PDRs on the surfaces of molecular gas clouds (e.g., Crawford et al. 1985; Stacey et al. 1985, 1991; Shibai et al. 1991; Wright et al. 1991).

#### 4.4. PDR Model

The PDR model put forth by Tielens & Hollenbach (1985a) and refined by Kaufman et al. (1999) has shown good agreement with observations for a wide variety of astrophysical environments (e.g., Hollenbach & Tielens 1997, 1999, and references therein). In their model, the PDR is taken as a homogeneous infinite plane slab of hydrogen nuclei density  $n_{\text{H}}$ , with an incident FUV ( $6 \text{ eV} < h\nu < 13.6 \text{ eV}$ ) flux parameterized in units of the local interstellar radiation field,  $G_0$  ( $1.6 \times 10^{-6} \text{ W m}^{-2}$ ; Habing 1968). The model assumes a number of fixed parameters, including the elemental, PAH, and dust abundances, absorption properties, and a Gaussian turbulent velocity field. The defining aspect of the model is the gas heating mechanism: about 10% of the incident FUV photons eject hot photoelectrons from the dust grains and PAH molecules, and these electrons collisionally heat the gas. The gas subsequently cools via FIR fine-structure line emission. The model is solved simultaneously for chemical and energy equilibrium in the slab, and the fine-structure emission of the various chemical species is predicted. Observed intensities of fine-structure lines can be compared with model results to constrain  $n_{\text{H}}$  and  $G_0$ .

We have modeled  $n_{\text{H}}$  and  $G_0$  over the 100 ISO raster positions in the Carina Nebula using the observed line intensities of  $63 \mu\text{m}$  [O I],  $146 \mu\text{m}$  [O I], and  $158 \mu\text{m}$  [C II] (Section 3.2), as well as the FIR intensity derived from a graybody fit to the entire LWS spectrum by Mizutani et al. (2004). (It is possible that the latter suffers a calibration error similar to those of the ISO spectra fit by Mizutani et al. 2002, 2004; see Section 3.2.) The  $158 \mu\text{m}$  [C II] intensities at each spatial position were corrected for the average fraction (63%; cf. Section 4.3) arising from the ionized medium—i.e., [C II] intensities were scaled by a factor of 0.63 at every spatial position. The calculations were performed with the online PDR Toolbox (PDRT; Pound & Wolfire 2008).<sup>6</sup> The standard set of model parameters was assumed (see Kaufman et al. 1999), and the calculator searched for the best fit of  $n_{\text{H}}$  and  $G_0$  to the combined observed intensity ratios of  $63/146 \mu\text{m}$  [O I],  $63/158 \mu\text{m}$  [O I]/[C II],  $146/158 \mu\text{m}$  [O I]/[C II], and  $(63+158)/\text{FIR}$ .

Our PDR model results are shown in Figure 14. The solution space of the PDRT is quantized in four equal divisions per decade on a logarithmic scale, resulting in recurrences of the same  $n_{\text{H}}$  and  $G_0$  values for several of the beam positions. To show this effect, circles are plotted around each data point, where the areas of the circles are proportional to the number of ISO raster positions yielding each solution. From the plot, we see that over most of the nebula  $10 \text{ cm}^{-3} < n_{\text{H}} < 1000 \text{ cm}^{-3}$  and  $10 < G_0 < 1000 \times 1.6 \mu\text{W m}^{-2}$ . The maximum is  $(n_{\text{H}}, G_0) = (31600, 5620)$ , but the average is (1250, 303). These data are near the low end of observed galactic star-forming regions, in which  $n_{\text{H}}$  and  $G_0$  are both typically  $\sim 10,000$  or more. The goodness of fit varies substantially from one data point to the next, but over the entire data set averages  $\sigma_{n_{\text{H}}} \sim 150 \text{ cm}^{-3}$  and  $\sigma_{G_0} \sim 40 \times 1.6 \mu\text{W m}^{-2}$ .

<sup>6</sup> <http://dustem.astro.umd.edu/pdrt/index.html>.

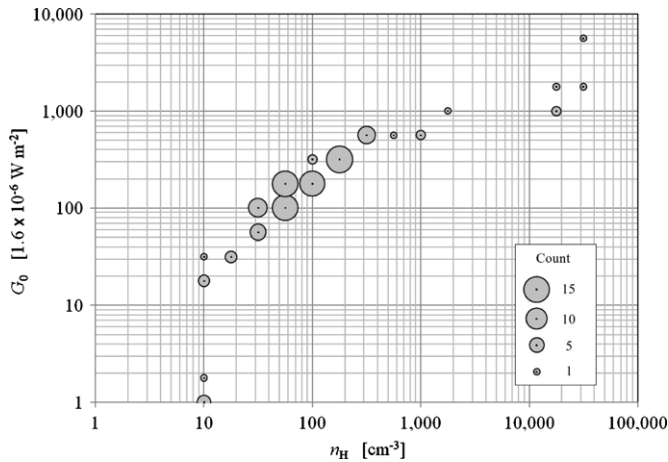


**Figure 14.** PDR model for Carina:  $G_0$  vs.  $n_H$ . The FUV ( $6\text{ eV} < E < 13.6\text{ eV}$ ) flux in units of the local interstellar radiation field,  $G_0$  ( $1.6 \times 10^{-6}\text{ W m}^{-2}$ ; Habing 1968), is plotted vs. the hydrogen nucleus density,  $n_H$  ( $\text{cm}^{-3}$ ), for the region of the Carina Nebula mapped by *ISO* (Figure 2). The data points were calculated using the PDR model of Kaufman et al. (1999) with the ratios of the *ISO* line intensities of 63 and  $146\text{ }\mu\text{m}$  [O I] and  $158\text{ }\mu\text{m}$  [C II] (from the present work), and the *ISO* FIR continuum intensity (from Mizutani et al. 2004). The calculations were performed with the online PDR Toolbox (PDRT; Pound & Wolfire 2008). Because the PDRT solution space is quantized (in four equal divisions per decade on a logarithmic scale), the relative areas of circles placed around each data point are used to indicate the number of raster positions (out of the 100 total observed by *ISO*) yielding each ( $n_H$ ,  $G_0$ ) solution.

The data of Figure 14 follow a clear trend, best fit by the power law  $G_0 = 4.84 n_H^{0.74}$ . This is somewhat in contrast to the correlation between  $G_0$  and  $n_H$  theoretically predicted by Young Owl et al. (2002) for a PDR in pressure equilibrium with

an ionization-bounded H II region, namely  $G_0 = 0.00804 n_H^{4/3}$ . At high densities ( $n_H \sim 6 \times 10^4\text{ cm}^{-3}$ ), both relations predict  $G_0 \sim 17,000$ . But at low densities ( $< 200\text{ cm}^{-3}$ ), we find a much ( $> 10$  times) higher  $G_0$  at a given  $n_H$ . Larger  $G_0$  at a given  $n_H$  means the star is much closer to the cloud than would be expected for an ionization-bounded H II region in pressure equilibrium with the PDR. The obvious solution is that the widespread H II regions in the Carina Nebula are not ionization-bounded, but rather well into the density-bounded stage so that the conditions of pressure equilibrium no longer apply. Establishing pressure equilibrium is relatively quick compared to the lifetime of the H II regions. For example, at the  $\sim 10\text{ km s}^{-1}$  sound speed, changes in pressure equilibrium across a  $1\text{ pc}$  H II region take about  $10^5\text{ yr}$ .

Of the five highest density data points in Figure 14, three (*ISO* raster beams Car 4-17, 4-21, and 4-23; see Table 4) are found in close proximity to Car II. Car II has a higher average ratio of 63/158 than elsewhere in the nebula (Table 2), suggesting the possibility of shocks (cf. Section 4.1.2). In particular, the 63/158 ratio at position Car 4-23 ( $(l, b) = (287.605, -0.636)$ ) is 1.35, about two times higher than average. Furthermore, the  $35\text{ }\mu\text{m}$  [Si II] line, measured by Mizutani et al. (2004), has an intensity at this position which is  $> 3.5$  times higher than average. The [Si II] line is a good tracer of shocks since shocks can strip silicon atoms off of dust grains. These shocks are likely the result of winds from  $\eta$  Car (or other massive members of Tr 16).

The modeled  $G_0$  and  $n_H$  values have been plotted spatially as contours in Figures 15 and 16. Quantitative averages of  $G_0$  and  $n_H$  over six spatial subregions of the nebula (corresponding to the sources Car I and II, Tr 14 and 16,  $\eta$  Car, and the GMC) are listed in Table 2 (Section 4.6). The morphology of the  $G_0$

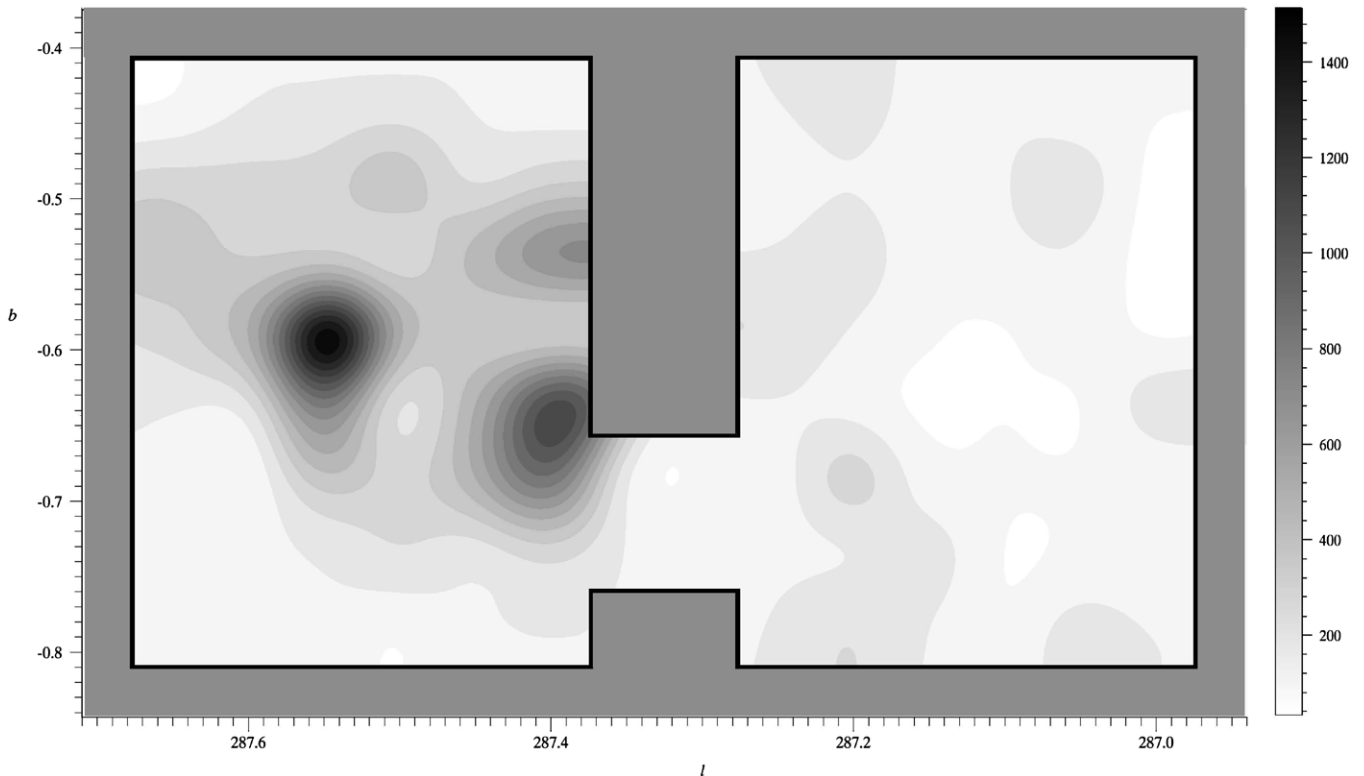


**Figure 15.** FUV radiation field ( $G_0$ ) map of the Carina Nebula. The FUV ( $6\text{ eV} < E < 13.6\text{ eV}$ ) flux in the units of the local interstellar radiation field,  $G_0$  ( $1.6 \times 10^{-6}\text{ W m}^{-2}$ ) is mapped over the Carina Nebula. Contour levels are shown every 5% of the peak flux (1514). The map has been resampled and smoothed with a Gaussian filter of  $\text{FWHM} = 79''/3$ , the average LWS beam.

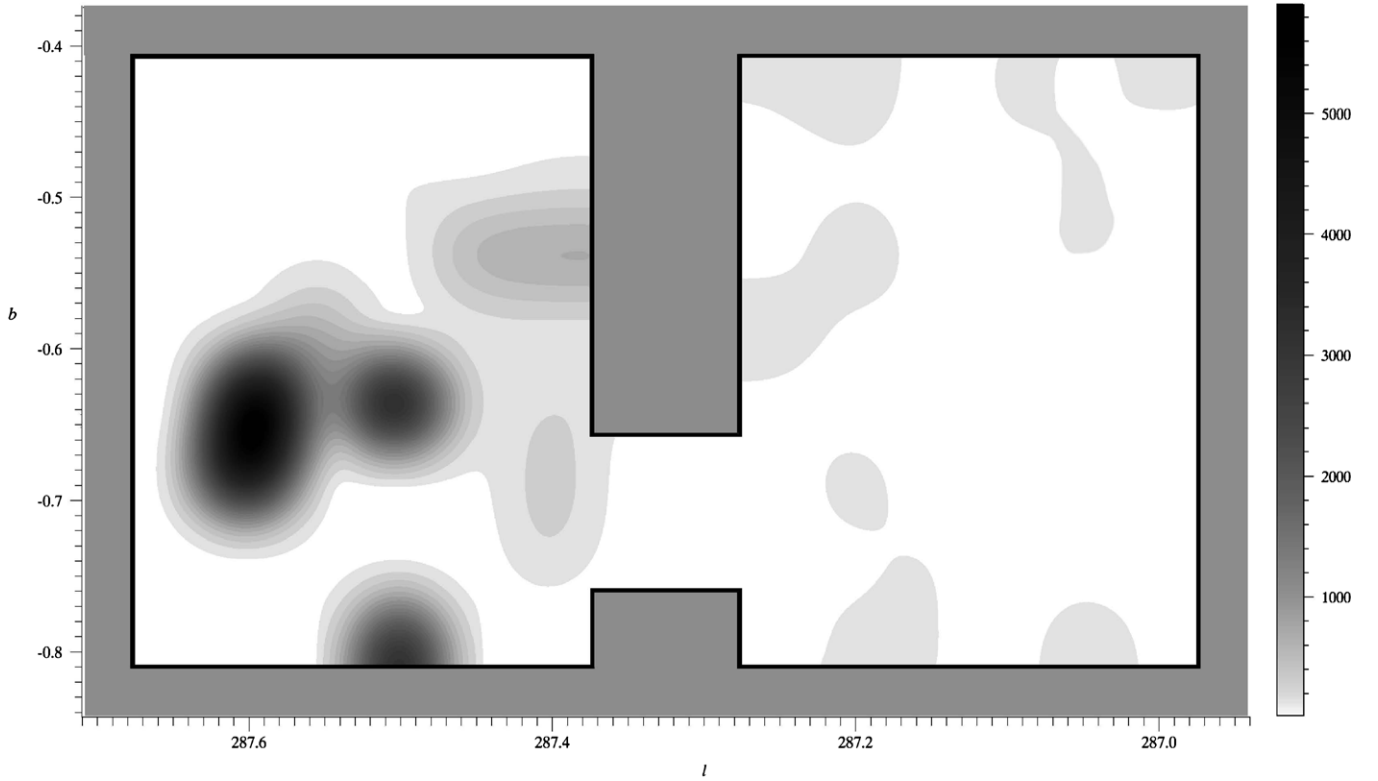


**Figure 16.**  $n_{\text{H}}$  map of the Carina Nebula. The hydrogen nuclei density,  $n_{\text{H}}$ , in units of  $\text{cm}^{-3}$ , is mapped over the Carina Nebula. Contour levels are shown every 2.5% of the peak density ( $5905 \text{ cm}^{-3}$ ). The map has been resampled and smoothed with a Gaussian filter of  $\text{FWHM} = 79''.3$ , the average LWS beam.

**Table 2**  
Parameters Averaged over Major Sources within the Carina Nebula

Parameter	Tr 16	$\eta$ Car	Car II	Tr 14	Car I	GMC	Entire Nebula <sup>a</sup>	Units
$l^b$	287.63	287.5969	287.56	287.40	287.37	<287.33	...	deg
$b$	-0.65	-0.6295	-0.61	-0.58	-0.63	...	...	deg
Measured parameters:								
$I$ ([O I] $63 \mu\text{m}$ )	15.0	30.8	57.5	81.2	79.2	12.6	13.4	$10^{-8} \text{ W m}^{-2} \text{ sr}^{-1}$
$I$ ([N II] $122 \mu\text{m}$ )	6.9	17.3	13.7	6.6	19.8	2.9	3.7	$10^{-8} \text{ W m}^{-2} \text{ sr}^{-1}$
$I$ ([O I] $146 \mu\text{m}$ )	0.6	1.2	2.4	3.2	6.4	0.6	0.7	$10^{-8} \text{ W m}^{-2} \text{ sr}^{-1}$
$I$ ([C II] $158 \mu\text{m}$ )	28.3	32.1	46.7	83.5	80.8	27.8	29.2	$10^{-8} \text{ W m}^{-2} \text{ sr}^{-1}$
$I$ ([N II] $205 \mu\text{m}$ )	12.3	< 2.6	16.2	12.2	18.7	9.5	11.3	$10^{-8} \text{ W m}^{-2} \text{ sr}^{-1}$
RV ([N II] $205 \mu\text{m}$ )	-34.7	...	-30.4	-32.2	-24.8	-27.9	-31.6	$\text{km s}^{-1}$
$\Gamma$ ([N II] $205 \mu\text{m}$ )	52.8	...	55.3	47.1	40.9	35.6	37.7	$\text{km s}^{-1}$
Derived parameters:								
% [C II] from PDRs	41	45	39	75	43	73	63	%
$G_0$	119	<10	3310	580	1390	152	303	$1.6 \mu\text{W m}^{-2}$
$n_{\text{H}}$ (PDRs)	78	17800	918	685	316	104	1250	$\text{cm}^{-3}$
$n_e$ (H II regions)	7	79	18	17	24	18	28	$\text{cm}^{-3}$
$N_{\text{H}}$ (PDRs)	417	70	46	184	356	180	31	$10^{20} \text{ cm}^{-2}$
$N_e$ (H II regions)	22	6	18	9	19	4	3	$10^{20} \text{ cm}^{-2}$
$T_{\text{surface}}$ (PDRs)	263	71	432	295	486	332	234	K
$\epsilon$ ([O I] $63 + [\text{C II}] 158/\text{FIR}$ )	2.8	...	1.5	3.7	2.7	4.3	3.4	$10^{-3}$

**Notes.**

<sup>a</sup> The “entire nebula” consists of all the observed raster positions, which differ between the *ISO* and SPIFI data (Figure 2).

<sup>b</sup> Coordinates refer to the nominal centers of the sources, listed in order of decreasing  $l$  (Röser & Bastian 1988 for  $\eta$  Car, Whiteoak 1994 for Car I and II, and Kharchenko et al. 2005 for Tr 14 and 16). The areas of the sources (over which the parameters were averaged) were determined by a multi-wavelength comparison with previous observations and are limited by the observed raster positions (see Table 6).

distribution roughly follows the PDR emission (Figures 6, 8, and 9) with the  $G_0$  fields peaking near the positions of Car I, Car II/ $\eta$  Car, and just north of Tr 14. The strongest  $G_0$  is found in the vicinity of Car II, as would be expected from the collection of massive early-type stars there ( $\eta$  Car and Tr 16). Little  $G_0$

flux is seen westward of  $l \sim 287.3$ , in the GMC. In its lower level contours,  $n_{\text{H}}$  shows a similar morphology to  $G_0$ . However, the eastern peaks (in the vicinity of  $\eta$  Car and Car II) are significantly larger relative to those at Car I and Tr 14. One explanation is the proximity of the dense Homunculus nebula



and Car II molecular cloud remnant to the strong  $G_0$  flux in these locations, so relatively higher density PDRs might be expected near these sources.

As a check on our PDR model for Carina (Section 4.4), it is instructive to compare the FUV flux predicted by the model with the FUV flux expected from the total luminosity of the nebula's known O and B spectral-type stars. It is now generally accepted—and further supported by the present work—that Car I is excited externally by the Tr 14 cluster to its northeast, and that Car II is excited externally by the Tr 16 cluster to its southeast. The O and B members of Tr 14 have a total FUV luminosity of  $L_{\text{FUV}} = 7.84 \times 10^{32}$  W (Smith 2006a), and the distance from Tr 14 to Car I is  $d \sim 2.34$  pc  $= 7.22 \times 10^{16}$  m (using the nominal source center positions from Table 2). Therefore, the expected FUV flux at Car I is  $G_0 = L_{\text{FUV}}/(4\pi d^2) \sim 7480 \times 1.6 \mu\text{W m}^{-2}$ . The O and B stars of Tr 16 have a combined FUV luminosity of  $L_{\text{FUV}} = 2.37 \times 10^{33}$  W, and a distance to Car II of  $d \sim 3.24$  pc  $= 10.0 \times 10^{16}$  m. Therefore, the expected FUV flux at Car II is  $G_0 = L_{\text{FUV}}/(4\pi d^2) \sim 11800 \times 1.6 \mu\text{W m}^{-2}$ .

For both Car I and II, the expected FUV flux from O and B stars (7480 and 11800, respectively) is a few times larger than the FUV flux predicted by our PDR model (1390 and 3310, respectively; Table 2). Thus, our findings agree with the established hypothesis that there is more than enough radiation from the O and B members of Tr 14 and 16 to externally excite Car I and II, respectively, without the need invoke embedded sources.

#### 4.5. Kinematics

Previous kinematic studies of the Carina Nebula have consistently found two large-scale effects.

1. Spectral lines near Car II show strong line splitting, while spectral lines near Car I are single-profiled. The double-peak profiles near Car II have been interpreted as arising from an expanding bubble of hot ionized gas, likely centered on Tr 16 or  $\eta$  Car. Car I, on the other hand, which shows only single spectral profiles, has been interpreted as an H II region which is expanding only into the GMC which wraps beneath and behind it (mostly receding along our line of sight), while the foreground is largely devoid of gas and dust (see Figure 11). Using the highly spectrally resolved radio recombination line observations of Huchtmeier & Day (1975), we estimate the average centroids of the two peaks of the nebula's double-peaked profiles near Car II to occur at  $-32.5 \text{ km s}^{-1}$  and  $-5.4 \text{ km s}^{-1}$ , with an average peak separation of  $27.1 \text{ km s}^{-1}$  and average individual peak width of  $27.9 \text{ km s}^{-1}$ . The single-profiled peaks near Car I have an average width of  $45.0 \text{ km s}^{-1}$ . Line splitting near Car II has also been observed by Zhang et al. (2001, in the submm lines of  $^{12}\text{CO}(4 \rightarrow 3)$  and [CI]), Deharveng & Maucherat (1975, in several optical lines), and Gardner et al. (1970, in several radio recombination lines).
2. Radial velocities measured near Car II are more negative than those near Car I (for the split profiles, the radial velocity referred to here is the average centroid of the two peaks). Thus, it appears that Car II is approaching slightly faster than Car I along our line of sight. Huchtmeier & Day (1975) report a radial velocity of  $\sim -24 \text{ km s}^{-1}$  at Car II and  $\sim -16 \text{ km s}^{-1}$  at Car I, with a monotonic gradient between the two positions. Velocity channel maps of the radio recombination line observations of Brooks et al.

(2001) show peak emission in Car II in the velocity channel centered at  $-28 \text{ km s}^{-1}$ , and peak emission in Car I in the velocity channel centered at  $-16 \text{ km s}^{-1}$  (the velocity resolution of these channel maps is  $4 \text{ km s}^{-1}$ ).

SPIFI cannot spectrally resolve the line splitting discussed above. However, one might expect unresolved (single-profile)  $205 \mu\text{m}$  [N II] peaks at Car II, which are wider than single-profile peaks elsewhere in the nebula. In particular, one might expect line widths near Car II of  $27.9 \text{ km s}^{-1}$  (the average width per peak in the split radio profiles)  $+ 27.1 \text{ km s}^{-1}$  (the average peak separation in the split radio profiles)  $= 55.0 \text{ km s}^{-1}$ . Near Car I, on the other hand, we might expect to see line widths similar to the average radio line width at Car I of  $45.0 \text{ km s}^{-1}$ . After de-convolving the spectral and instrument profiles to recover the intrinsic line widths (Oberst 2009), the  $205 \mu\text{m}$  [N II] SPIFI data yield an average intrinsic line width of  $55.3 \text{ km s}^{-1}$  at Car II and  $40.9 \text{ km s}^{-1}$  at Car I (Table 2), in good agreement with the radio data.

Furthermore, we find the average radial velocities of the  $205 \mu\text{m}$  [N II] lines near Car I and Car II to be  $-24.8 \text{ km s}^{-1}$  and  $-30.4 \text{ km s}^{-1}$ , respectively (Table 2). (Average line widths and velocities for other regions of the nebula can also be found in Table 2.) These values are somewhat more negative than the average velocities of the radio data of Huchtmeier & Day (1975,  $-16 \text{ km s}^{-1}$  and  $-24 \text{ km s}^{-1}$ , respectively). However, both data sets are in agreement that Car II is approaching slightly faster than Car I along our line of sight. It is likely that this  $\sim -7.5 \text{ km s}^{-1}$  ( $\sim 10\%$  of an SPIFI resolution element) blueshift of the SPIFI data relative to the radio data is the result of imperfect velocity calibration in our system (see Section 2.1). Taking into account such effects, the radial velocities observed in the SPIFI data are in very good agreement with those of the radio data.

#### 4.6. Comparison of Sources

To compare the contributions from various sources within Carina to one another and to other Galactic and extragalactic sources, we have averaged our data over six spatial subregions of the nebula corresponding to the sources Car I and II, Tr 14 and 16,  $\eta$  Car, and the westerly GMC. The results are shown in Table 2, where the sources are listed in order of decreasing galactic longitude,  $l$ . We have also included averages over the whole nebula. With the exception of  $\eta$  Car, all of these sources are extended relative our beam sizes, and thus had to be averaged over several beams in both the SPIFI and ISO rasters. The raster beams assigned to each source were chosen by proximity to the nominal central position of the source (Table 2) and multi-wavelength morphological considerations (Section 4.1). The beam assignments are listed in Table 6. Given the coarse spatial sampling of both SPIFI and ISO, and the lack of strictly defined boundaries for extended sources in general, there is some subjectivity in these assignments. However, the results of Table 2 are not overly sensitive to them.

For each of the sources within Carina, Table 2 lists the average measured line intensities ( $I$ ) of the spectral species observed by SPIFI and ISO (Sections 3.1 and 3.2) and the average measured radial velocities (RV) and intrinsic line widths ( $\Gamma$ ) of the  $205 \mu\text{m}$  [N II] lines (Section 4.5). In addition to these measured parameters, Table 2 includes averages of several derived parameters: the electron density ( $n_e$ , Section 4.2); the percentage of the  $158 \mu\text{m}$  [C II] emission arising from PDRs (Section 4.3); and the FUV flux ( $G_0$ ), hydrogen nuclei density

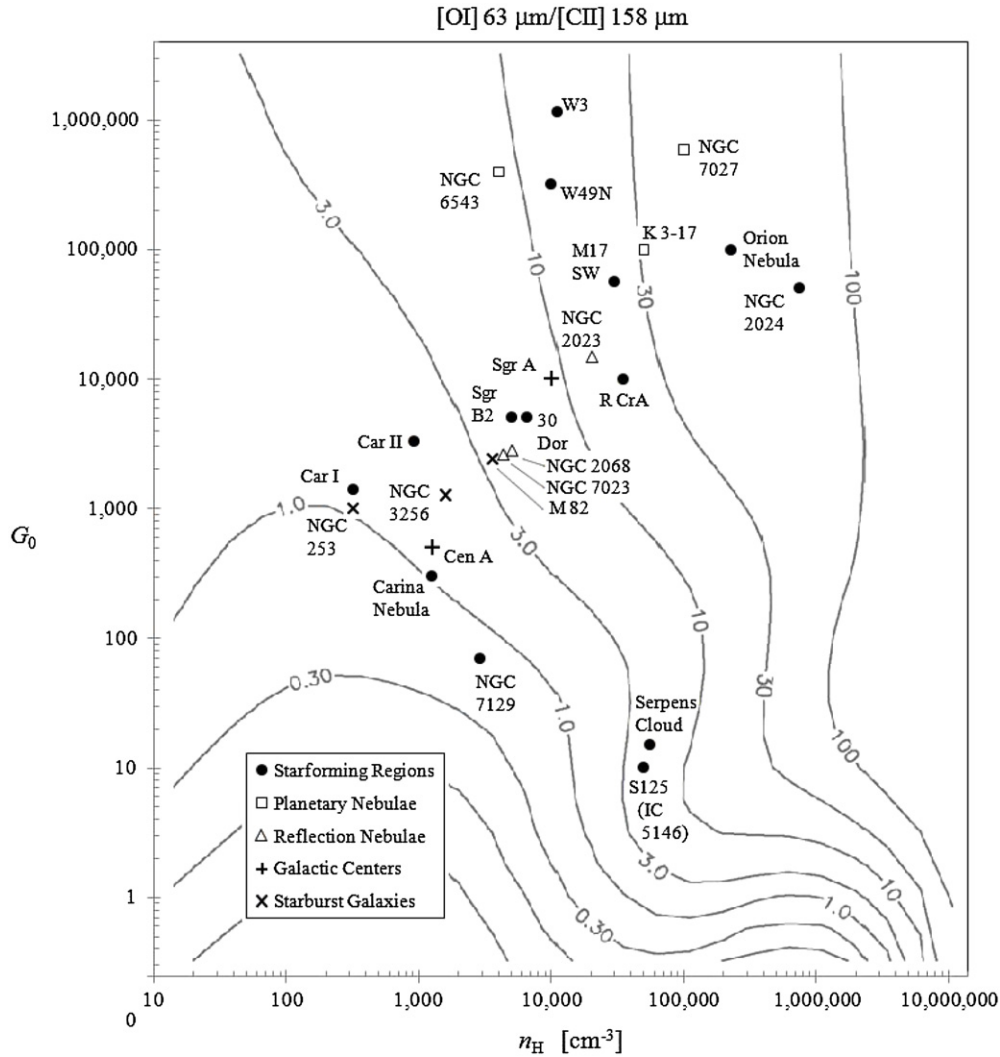


**Figure 17.** Comparison of PDRs in astrophysical sources. The PDR properties ( $n_{\text{H}}$  and  $G_0$ ) of Car I, Car II, and the entire Carina Nebula (Table 2) are compared to other Galactic and extragalactic sources. The contours show the line intensity ratio of  $63\ \mu\text{m}$  [OI] to  $158\ \mu\text{m}$  [CII] (taken from Kaufman et al. 1999). References: Orion Nebula, Tielens & Hollenbach (1985b); M17 SW, Meixner et al. (1992); R CrA, Giannini et al. (1998); NGC 7129, Tommasi et al. (1998); Sgr A and NGC 7027, Hollenbach & Tielens (1999); NGC 2024, Giannini et al. (2000); Cen A, Negishi et al. (2001) and Unger et al. (2000); M 82, NGC 253, and NGC 3256, Negishi et al. (2001); 30 Dor, Vastel et al. (2001) and Poglitsch et al. (1995); W49N, Vastel et al. (2001); Serpens Cloud, Larsson et al. (2002); NGC 2023, NGC 2068, and NGC 7023, Young Owl et al. (2002); S125 (IC 5146), Aannestad & Emery (2003); Sgr B2, Goicoechea et al. (2004); W3, Kramer et al. (2004); K 3-17 and NGC 6543, Bernard-Salas & Tielens (2005).

( $n_{\text{H}}$ ), PDR surface temperature ( $T_{\text{surface}}$ ), and photoelectric heating efficiency ( $\epsilon$ , Section 4.4).

Finally, we have calculated the hydrogen and electron column densities,  $N_{\text{H}}$  and  $N_{\text{e}}$ , for PDRs and H II regions, respectively, using the measured intensities of  $146\ \mu\text{m}$  [OI] for PDRs (since this line is typically optically thin) and  $122\ \mu\text{m}$  [NII] for H II regions. We assumed a PDR temperature equal to the PDR surface temperature (which will be higher than that in the bulk of the PDR), so that our column densities for PDRs are likely to be underestimates. From these column densities we find a relative mass fraction for PDRs/(PDRs + H II regions) of  $\sim 91\%$ – $98\%$  for all sources except Car II, where it is  $72\%$ . Thus, despite the fact that the [CII] emission from PDRs is only  $\sim 2$  times greater than that from H II regions, the mass of PDR gas greatly exceeds that of ionized gas. This is not surprising, as it takes very little ionized gas to produce nearly as much [CII] emission as arises from the neutral gas. This is because the collision strengths for the electron/ion-impact excitation of [CII] in H II regions are much greater than those in the neutral gas regions. These large

PDR/H II region mass ratios are reminiscent of the high ratios observed in the Galaxy as a whole and in external galaxies (cf. Crawford et al. 1985; Stacey et al. 1985, 1991).

In Figure 17, we have plotted the data for Car I, Car II, and the entire Carina Nebula (taken from Table 2) on  $n_{\text{H}}$  and  $G_0$  axes with several other Galactic and extragalactic sources. The data points are overlaid on contours of the line intensity ratio of  $63\ \mu\text{m}$  [OI] to  $158\ \mu\text{m}$  [CII] from the PDR model of Kaufman et al. (1999). The Carina sources have lower densities and FUV fields ( $n_{\text{H}} < 10^4$  and  $G_0 < 10^4$ ) than most other Galactic star-forming regions—e.g., the Orion Nebula, M17, and W49. Instead, Carina may be more akin to 30 Doradus (as previously suggested by Brooks et al. 2003).

The physical separation between Tr 14 and the Car I PDR is similar to the distance between the [CII] peak and star cluster R136 in 30 Dor (Israel et al. 1996). In both of these regions, the bulk of the molecular matter in the vicinity of the early-type stars has been destroyed or swept away, and the PDRs we see are forming on the peripheral edges of the remaining GMCs.

On the other hand, in the case of Orion, the parent molecular cloud (OMC-1) still appears to be relatively intact, resulting in PDRs which have formed much closer to the exciting stars. We also notice that the conditions in Carina are similar to those in large ( $\sim 500$  pc scale) beam studies of the nearby starburst galaxies NGC 253, NGC 3256, and M82. The very high rates of star formation over large scales in Carina have resulted in FUV fields and gas excitation conditions that mimic those in starburst galaxies as a whole.

## 5. SUMMARY

We present new observations and analysis of several FIR and submm spectral lines in the Carina Nebula. These observations have enabled us to map the neutral and ionized gas components of the nebula to spatial resolutions of  $\sim$  few arcminutes. From these spectral data, we have derived electron and hydrogen densities and column densities, the fraction of  $C^+$  arising from PDRs, FUV fluxes, radial velocities, PDR surface temperatures, and photoelectric heating efficiencies.

Our study supports the following key conclusions.

1. The Carina Nebula contains two main regions of ionized gas emission (i.e., H II regions): Car I, lying  $\sim \frac{1}{2}$  pc southwest of Tr 14, and Car II, lying  $\sim \frac{1}{2}$  pc west of Tr 16. Enhanced neutral gas emission is found primarily along the south and west edges of Car I, and also behind Car I along our line of sight. Because Carina's GMC butts against Car I to the south and west and also wraps behind it along our line of sight, this neutral emission very likely arises from the photodissociated surface of this cloud (i.e., from PDRs).
2. The H II regions and PDRs of the nebula are powered externally by the intense UV radiation fields from Tr 14 and 16—in some cases from up to a few parsecs away.
3. Relative to the nebula, ionized gas in the vicinity of Tr 16 seems to be expanding outward in all directions in a bubble-like fashion. The ionized component near Tr 14, on the other hand, appears to be devoid of foreground gas but is expanding into the background neutral and molecular gas that wraps behind Tr 14 along our line of sight (a half-bubble). Furthermore, the eastern half of the nebula (Tr 16 and Car II) is approaching slightly faster than the western half (Tr 14 and Car I) along our line of sight.
4. The ionized gas is very diffuse:  $n_e \lesssim 100 \text{ cm}^{-3}$ . Furthermore, this density does not vary significantly over the nebula, even outside the regions of enhanced ionized gas emission (i.e., outside of Car I and II). Therefore, it appears that the entire ( $\sim 30$  pc across) nebula has a diffuse ionized component that is either intermixed with other gas phases or which blankets (or “halos”) the entire region.
5. The majority ( $\sim \frac{2}{3}$ ) of  $C^+$  emission in the Carina Nebula arises from PDRs. Thus,  $C^+$  is a tracer of neutral, rather than ionized, gas. Furthermore, this fraction serves as an important scaling parameter when entering  $C^+$  line intensities into PDR models.
6. PDR modeled values of  $G_0$  and  $n_H$  suggest that Carina is more akin to larger and more evolved star-forming regions such as 30 Doradus in the LMC than any of the well-known nearby star-forming regions in the Milky Way. The very high rates of star formation over large scales in Carina even appear to mimic the conditions in some starburst galaxies as a whole.

Finally, our  $205 \mu\text{m}$  data constitute the first ground-based detection of the  $205 \mu\text{m}$  [N II] line, and only the third detection overall since those of the *COBE* FIRAS and the KAO in the early 1990s. *COBE*'s all-sky map of [N II]  $205 \mu\text{m}$  used a very broad ( $7^\circ$ ) beam, and hence only probes the warm ionized medium (WIM) on galactic scales (Wright et al. 1991; Bennett et al. 1994; Fixsen et al. 1999). Pioneering efforts by the KAO team resulted in the first detection of  $205 \mu\text{m}$  [N II] in discrete H II regions, but these spectra are few and do not map the detailed spatial structure of [N II] emission within these sources (Colgan et al. 1993; Petuchowski et al. 1994, 1996; Simpson et al. 1997, 2004). Thus, the present data comprise the first extended, medium resolution ( $\sim 1'$ ) map of  $205 \mu\text{m}$  [N II] over a star-forming region, offering a unique opportunity to compare the  $205 \mu\text{m}$  emission to the  $122 \mu\text{m}$  [N II] line and other tracers of the WIM in Carina and other similar regions.

The authors especially thank the following individuals and groups: Carole E. Tucker, who provided SPIFI's filters; Jacob W. Kooi, for operating local oscillators at the AST/RO during SPIFI calibration; K. Sigfrid Yngvesson and the TREND group, for use of the TREND laser at the AST/RO during SPIFI calibration; and prior members of the SPIFI team, including C. Matt Bradford, Alberto D. Bolatto, James M. Jackson, Mark R. Swain, Maureen L. Savage, Jacqueline A. Davidson, and  $\sim 15$  undergraduate student researchers. Finally, we are thankful for the support of the following grants: NASA GSRP NNG05GK70H; NSF IGERT DGE-9870631; NSF CSIP DGE-0231913; and NSF OPP-0094605, OPP-0338149, and OPP-0126090.

*Facilities:* AST/RO (SPIFI), ISO (LWS)

## APPENDIX

**Table 3**  
SPIFI  $205 \mu\text{m}$  [N II] Line Intensities

Raster Beam <sup>a</sup>	Galactic Coordinates <sup>a</sup> (deg)		Line Intensity <sup>b</sup> ( $10^{-8} \text{ W m}^{-2} \text{ sr}^{-1}$ )	
	<i>l</i>	<i>b</i>	<i>I</i>	( $\sigma_I$ )
1	287.3973	−0.7445	18.0	(5.8)
2	287.4010	−0.7267	< 4.4	
3	287.4048	−0.7089	< 9.4	
4	287.4086	−0.6911	< 3.8	
5	287.4123	−0.6734	< 2.5	
6	287.4161	−0.6556	< 12.8	



**Table 3**  
(Continued)

Raster Beam <sup>a</sup>	Galactic Coordinates <sup>a</sup> (deg)		Line Intensity <sup>b</sup> ( $10^{-8} \text{ W m}^{-2} \text{ sr}^{-1}$ )	
	$l$	$b$	$I$	( $\sigma_I$ )
7	287.4199	-0.6378	<8.5	
8	287.4237	-0.6200	25.5	(4.3)
9	287.4276	-0.6022	<5.9	
10	287.3795	-0.7407	<4.5	
11	287.3832	-0.7229	...	
12	287.3870	-0.7051	<2.9	
13	287.3908	-0.6873	16.4	(5.4)
14	287.3946	-0.6696	<4.5	
15	287.3983	-0.6518	...	
16	287.4021	-0.6340	<6.3	
17	287.4060	-0.6162	<14.3	
18	287.4098	-0.5984	...	
19	287.3543	-0.7725	<8.3	
20	287.3580	-0.7547	<1.5	
21	287.3617	-0.7369	8.6	(1.7)
22	287.3655	-0.7191	12.8	(4.1)
23	287.3692	-0.7014	<8.8	
24	287.3730	-0.6836	29.3	(4.1)
25	287.3768	-0.6658	16.7	(3.1)
26	287.3806	-0.6480	33.1	(6.9)
27	287.3844	-0.6302	51.7	(11.0)
28	287.3882	-0.6124	42.8	(9.1)
29	287.3920	-0.5946	23.1	(3.2)
30	287.3365	-0.7687	<7.2	
31	287.3402	-0.7509	<10.3	
32	287.3440	-0.7332	<3.5	
33	287.3477	-0.7154	<7.6	
34	287.3514	-0.6976	32.9	(3.9)
35	287.3552	-0.6798	10.8	(1.9)
36	287.3590	-0.6620	31.8	(5.8)
37	287.3628	-0.6442	30.5	(7.5)
38	287.3665	-0.6264	25.3	(8.6)
39	287.3704	-0.6086	13.9	(4.3)
40	287.3742	-0.5908	<7.7	
41	287.3187	-0.7650	17.2	(4.0)
42	287.3224	-0.7472	25.7	(7.2)
43	287.3262	-0.7294	<2.9	
44	287.3299	-0.7116	26.0	(3.0)
45	287.3337	-0.6938	14.2	(1.9)
46	287.3374	-0.6760	21.4	(2.2)
47	287.3412	-0.6582	26.8	(5.2)
48	287.3450	-0.6404	<1.8	
49	287.3487	-0.6226	20.2	(6.7)
50	287.3525	-0.6048	23.7	(5.4)
51	287.3564	-0.5870	<5.5	
52	287.3009	-0.7612	13.0	(2.4)
53	287.3047	-0.7434	12.8	(3.6)
54	287.3084	-0.7257	23.2	(6.0)
55	287.3121	-0.7079	<1.5	
56	287.3159	-0.6901	34.7	(6.0)
57	287.3196	-0.6723	6.7	(1.5)
58	287.3234	-0.6545	<2.1	
59	287.3271	-0.6367	<2.3	
60	287.3309	-0.6189	31.7	(4.4)
61	287.3347	-0.6011	<3.4	
62	287.3385	-0.5833	...	
63	287.2832	-0.7575	3.5	(1.0)
64	287.2869	-0.7397	23.4	(5.6)
65	287.2906	-0.7219	<8.5	
66	287.2943	-0.7041	<1.5	
67	287.2981	-0.6863	<1.9	

**Table 3**  
(Continued)

Raster Beam <sup>a</sup>	Galactic Coordinates <sup>a</sup> (deg)		Line Intensity <sup>b</sup> ( $10^{-8} \text{ W m}^{-2} \text{ sr}^{-1}$ )	
	$l$	$b$	$I$	( $\sigma_I$ )
68	287.3018	-0.6685	6.6	(1.1)
69	287.3056	-0.6507	19.7	(4.2)
70	287.3093	-0.6329	7.1	(2.0)
71	287.3131	-0.6151	11.0	(3.2)
72	287.3169	-0.5973	<2.5	
73	287.3207	-0.5795	24.6	(7.3)
74	287.2654	-0.7538	14.2	(3.5)
75	287.2691	-0.7360	15.4	(4.1)
76	287.2728	-0.7182	<2.7	
77	287.2765	-0.7004	<3.2	
78	287.2802	-0.6826	<2.1	
79	287.2840	-0.6648	11.4	(2.6)
80	287.2878	-0.6470	<3.8	
81	287.2915	-0.6292	<2.6	
82	287.2953	-0.6113	15.1	(2.8)
83	287.2991	-0.5935	<13.1	
84	287.3029	-0.5757	<14.0	
85	287.2476	-0.7501	<8.9	
86	287.2513	-0.7323	<13.1	
87	287.2550	-0.7145	10.0	(1.7)
88	287.2587	-0.6967	<3.3	
89	287.2624	-0.6788	40.9	(8.0)
90	287.2662	-0.6610	<2.9	
91	287.2699	-0.6432	25.2	(7.4)
92	287.2737	-0.6254	26.2	(5.9)
93	287.2775	-0.6076	8.8	(1.8)
94	287.2813	-0.5898	<4.8	
95	287.2851	-0.5720	<4.9	
96	287.2889	-0.5542	<2.6	
97	287.2927	-0.5363	<12.2	
98	287.2298	-0.7464	<5.6	
99	287.2335	-0.7286	<14.0	
100	287.2372	-0.7108	<9.5	
101	287.2409	-0.6929	<6.1	
102	287.2446	-0.6751	<13.2	
103	287.2484	-0.6573	<19.1	
104	287.2521	-0.6395	<9.2	
105	287.2559	-0.6217	<13.8	
106	287.2596	-0.6039	38.1	(11.0)
107	287.2634	-0.5861	<15.2	
108	287.2672	-0.5682	<5.2	
109	287.2710	-0.5504	<13.5	
110	287.2748	-0.5326	...	
111	287.2268	-0.6714	18.4	(4.1)
112	287.2305	-0.6536	<2.8	
113	287.2343	-0.6358	<6.7	
114	287.2380	-0.6180	<8.3	
115	287.2418	-0.6002	<3.1	
116	287.2456	-0.5823	13.6	(3.8)
117	287.2494	-0.5645	<13.9	
118	287.2532	-0.5467	<4.1	
119	287.2570	-0.5289	18.1	(3.7)
120	287.2090	-0.6677	14.6	(3.4)
121	287.2127	-0.6499	<8.7	
122	287.2164	-0.6321	<7.6	
123	287.2202	-0.6143	<12.1	
124	287.2240	-0.5964	<7.2	
125	287.2277	-0.5786	<10.4	
126	287.2315	-0.5608	45.5	(10.8)
127	287.2353	-0.5430	<4.5	
128	287.2391	-0.5252	<14.1	
129	287.1911	-0.6640	13.3	(3.1)
130	287.1949	-0.6462	<5.6	

**Table 3**  
(Continued)

Raster Beam <sup>a</sup>	Galactic Coordinates <sup>a</sup> (deg)		Line Intensity <sup>b</sup> ( $10^{-8} \text{ W m}^{-2} \text{ sr}^{-1}$ )	
	$l$	$b$	$I$	$(\sigma_I)$
131	287.1986	−0.6284	<4.7	
132	287.2023	−0.6106	<10.7	
133	287.2061	−0.5927	<9.8	
134	287.2099	−0.5749	<5.9	
135	287.2136	−0.5571	<6.6	
136	287.2174	−0.5393	<8.1	
137	287.2212	−0.5214	<9.3	
138	287.6467	−0.6950	<12.9	
139	287.6506	−0.6772	<9.4	
140	287.6545	−0.6595	<5.9	
141	287.6584	−0.6417	<6.5	
142	287.6623	−0.6240	12.9	(5.6)
143	287.6663	−0.6062	14.9	(3.4)
144	287.6702	−0.5885	12.4	(3.3)
145	287.6742	−0.5707	<9.1	
146	287.6782	−0.5530	<5.5	
147	287.6289	−0.6910	11.3	(3.7)
148	287.6328	−0.6733	...	
149	287.6367	−0.6555	13.5	(2.8)
150	287.6407	−0.6378	<7.8	
151	287.6446	−0.6200	14.0	(4.1)
152	287.6485	−0.6023	<10.9	
153	287.6525	−0.5845	20.7	(5.9)
154	287.6564	−0.5668	<6.4	
155	287.6604	−0.5490	...	
156	287.6112	−0.6871	<6.4	
157	287.6151	−0.6693	7.8	(2.6)
158	287.6190	−0.6516	<4.1	
159	287.6229	−0.6338	14.5	(3.4)
160	287.6268	−0.6161	6.7	(1.7)
161	287.6308	−0.5983	20.1	(6.0)
162	287.6347	−0.5806	<3.8	
163	287.6386	−0.5629	<3.9	
164	287.6426	−0.5450	<4.0	
165	287.5935	−0.6832	17.1	(3.6)
166	287.5973	−0.6654	<12.3	
167	287.6012	−0.6477	11.4	(2.8)
168	287.6052	−0.6299	<2.6	
169	287.6091	−0.6121	22.2	(7.7)
170	287.6130	−0.5944	<2.5	
171	287.6170	−0.5766	10.1	(3.1)
172	287.6208	−0.5590	<6.4	
173	287.6248	−0.5411	<11.2	
174	287.5757	−0.6793	7.3	(1.1)
175	287.5796	−0.6615	10.9	(2.1)
176	287.5835	−0.6438	8.9	(1.5)
177	287.5874	−0.6260	6.8	(0.8)
178	287.5913	−0.6082	15.3	(2.2)
179	287.5953	−0.5904	13.8	(1.9)
180	287.5992	−0.5727	<3.5	
181	287.6030	−0.5551	<3.1	
182	287.6070	−0.5372	10.0	(2.7)
183	287.5580	−0.6754	7.0	(1.5)
184	287.5618	−0.6576	<6.1	
185	287.5657	−0.6398	16.5	(2.1)
186	287.5696	−0.6221	10.4	(2.1)
187	287.5736	−0.6042	24.4	(4.2)
188	287.5775	−0.5865	13.4	(3.3)
189	287.5814	−0.5688	12.3	(2.4)
190	287.5852	−0.5512	14.2	(3.5)
191	287.5892	−0.5332	<8.6	
192	287.5402	−0.6715	17.0	(2.6)
193	287.5441	−0.6537	11.9	(3.1)



**Table 3**  
(Continued)

Raster Beam <sup>a</sup>	Galactic Coordinates <sup>a</sup> (deg)		Line Intensity <sup>b</sup> ( $10^{-8} \text{ W m}^{-2} \text{ sr}^{-1}$ )	
	$l$	$b$	$I$	$(\sigma_I)$
194	287.5480	−0.6360	27.3	(4.0)
195	287.5519	−0.6182	27.4	(3.3)
196	287.5558	−0.6003	25.0	(4.6)
197	287.5598	−0.5825	12.1	(1.9)
198	287.5637	−0.5648	26.7	(4.7)
199	287.5674	−0.5473	<4.1	
200	287.5714	−0.5293	<3.0	
201	287.5224	−0.6676	<4.2	
202	287.5263	−0.6498	<5.4	
203	287.5302	−0.6321	16.9	(3.3)
204	287.5341	−0.6143	<2.5	
205	287.5381	−0.5963	<2.7	
206	287.5420	−0.5786	16.2	(1.8)
207	287.5459	−0.5609	<6.0	
208	287.5496	−0.5434	<5.2	
209	287.5536	−0.5254	<7.2	
210	287.5046	−0.6637	8.4	(2.8)
211	287.5085	−0.6460	17.6	(2.3)
212	287.5124	−0.6282	8.5	(1.9)
213	287.5164	−0.6104	<1.5	
214	287.5203	−0.5924	7.4	(1.8)
215	287.5243	−0.5746	6.9	(1.4)
216	287.5282	−0.5569	<4.0	
217	287.5318	−0.5395	<3.9	
218	287.5358	−0.5215	<3.2	
219	287.4869	−0.6599	<3.2	
220	287.4907	−0.6421	<17.0	
221	287.4946	−0.6243	<4.5	
222	287.4986	−0.6065	<5.0	
223	287.5026	−0.5884	19.3	(3.7)
224	287.5065	−0.5707	<6.1	
225	287.5104	−0.5530	<5.5	
226	287.5140	−0.5356	<2.3	
227	287.5180	−0.5176	<14.7	
228	287.4691	−0.6560	<7.4	
229	287.4729	−0.6382	<5.1	
230	287.4768	−0.6205	15.0	(3.8)
231	287.4809	−0.6026	<2.5	
232	287.4848	−0.5845	<4.0	
233	287.4888	−0.5667	<3.7	
234	287.4926	−0.5491	<4.4	
235	287.4962	−0.5317	<5.5	
236	287.5002	−0.5138	<10.6	

**Notes.**<sup>a</sup> Raster points and coordinates correspond to the SPIFI 54'' beam positions shown in Figure 2.<sup>b</sup> For spectra with  $\chi^2$  fits of  $S/N \lesssim 3$ , theoretical upper limits to intensity are given, as indicated by the “<” signs (see the text for more details). Intensity errors ( $\sigma_I$ ) do not include the SPIFI absolute calibration error of 26%. In a few rare cases, no intensity (or upper limit) is reported, indicating that only the nonfunctional SPIFI array pixels observed that position.**Table 4**  
ISO Observations of the Carina Nebula

Raster Beam <sup>a</sup>	Galactic Coordinates <sup>a</sup> (deg)		Line Intensities (10 <sup>−8</sup> W m <sup>−2</sup> sr <sup>−1</sup> ) <sup>b</sup>								
			(O I)		(N II)		(O I)		(C II)		
	63 μm		122 μm		146 μm		158 μm				
	<i>l</i>	<i>b</i>	<i>I</i>	(σ <sub><i>I</i></sub> )	<i>I</i>	(σ <sub><i>I</i></sub> )	<i>I</i>	(σ <sub><i>I</i></sub> )	<i>I</i>	(σ <sub><i>I</i></sub> )	
Car 1	1	287.006	−0.587	10.1	(0.2)	1.4	(0.2)	1.0	(0.1)	26.0	(0.3)
Car 1	2	287.056	−0.587	11.3	(0.2)	1.7	(0.2)	0.7	(0.1)	25.7	(0.3)
Car 1	3	287.106	−0.586	12.7	(0.3)	2.5	(0.3)	0.8	(0.1)	37.7	(0.3)

**Table 4**  
(Continued)

Raster Beam <sup>a</sup>		Galactic Coordinates <sup>a</sup> (deg)		Line Intensities [ $10^{-8} \text{ W m}^{-2} \text{ sr}^{-1}$ ] <sup>b</sup>							
				(O I) 63 $\mu\text{m}$		(N II) 122 $\mu\text{m}$		(O I) 146 $\mu\text{m}$		(C II) 158 $\mu\text{m}$	
		<i>l</i>	<i>b</i>	<i>I</i>	( $\sigma_I$ )	<i>I</i>	( $\sigma_I$ )	<i>I</i>	( $\sigma_I$ )	<i>I</i>	( $\sigma_I$ )
Car 1	4	287.156	−0.586	24.5	(0.6)	1.8	(0.4)	0.8	(0.1)	49.9	(1.0)
Car 1	5	287.206	−0.585	39.3	(0.6)	6.6	(0.4)	2.0	(0.2)	77.7	(1.9)
Car 1	6	287.256	−0.585	53.3	(0.6)	6.3	(0.4)	3.1	(0.3)	91.7	(2.3)
Car 1	7	287.006	−0.537	6.4	(0.2)	1.4	(0.1)	0.5	(0.1)	18.8	(0.5)
Car 1	8	287.056	−0.537	11.9	(0.4)	1.1	(0.2)	0.5	(0.1)	24.1	(0.3)
Car 1	9	287.106	−0.536	19.0	(0.3)	2.3	(0.3)	1.4	(0.1)	53.2	(1.3)
Car 1	10	287.156	−0.536	15.1	(0.3)	3.7	(0.2)	0.7	(0.1)	39.6	(0.4)
Car 1	11	287.206	−0.535	26.9	(0.7)	3.8	(0.2)	1.4	(0.1)	49.1	(0.8)
Car 1	12	287.256	−0.535	14.8	(0.4)	3.0	(0.2)	0.9	(0.1)	40.7	(0.5)
Car 1	13	287.005	−0.487	5.4	(0.3)	1.5	(0.1)	0.4	(0.1)	16.3	(0.5)
Car 1	14	287.055	−0.487	10.8	(0.4)	2.0	(0.1)	0.5	(0.1)	17.3	(0.2)
Car 1	15	287.105	−0.486	13.4	(0.4)	3.5	(0.2)	0.6	(0.1)	29.3	(0.3)
Car 1	16	287.155	−0.486	7.6	(0.3)	1.3	(0.1)	0.3	(0.1)	18.8	(0.4)
Car 1	17	287.205	−0.485	8.9	(0.3)	1.7	(0.1)	0.7	(0.1)	26.8	(0.3)
Car 1	18	287.255	−0.485	8.3	(0.3)	3.1	(0.3)	0.4	(0.1)	26.4	(0.4)
Car 1	19	287.005	−0.437	5.2	(0.3)	1.3	(0.1)	0.3	(0.1)	18.0	(0.4)
Car 1	20	287.055	−0.437	10.3	(0.3)	2.8	(0.2)	0.4	(0.1)	20.9	(0.3)
Car 1	21	287.105	−0.436	15.8	(0.4)	1.1	(0.2)	0.5	(0.1)	25.9	(0.3)
Car 1	22	287.155	−0.436	7.4	(0.2)	1.1	(0.1)	0.4	(0.1)	22.5	(0.2)
Car 1	23	287.205	−0.435	8.6	(0.3)	1.4	(0.1)	0.5	(0.1)	17.5	(0.4)
Car 1	24	287.255	−0.435	8.8	(0.3)	1.6	(0.1)	0.5	(0.1)	21.0	(0.3)
Car 2	1	287.405	−0.586	40.3	(1.0)	7.7	(0.5)	1.6	(0.2)	73.7	(1.5)
Car 2	2	287.455	−0.586	40.3	(0.6)	9.2	(0.3)	2.1	(0.2)	67.5	(1.6)
Car 2	3	287.505	−0.586	17.7	(0.9)	12.8	(0.8)	1.4	(0.2)	36.6	(0.4)
Car 2	4	287.555	−0.586	130.7	(2.2)	11.9	(0.6)	4.4	(0.3)	56.3	(0.6)
Car 2	5	287.605	−0.586	10.8	(0.6)	7.4	(0.3)	1.1	(0.1)	27.7	(0.4)
Car 2	6	287.655	−0.586	7.6	(0.4)	6.0	(0.3)	0.7	(0.1)	28.0	(0.3)
Car 2	7	287.405	−0.536	148.9	(1.7)	6.2	(0.4)	6.9	(0.4)	92.2	(2.3)
Car 2	8	287.455	−0.536	116.3	(1.2)	5.9	(0.5)	4.6	(0.4)	95.5	(2.1)
Car 2	9	287.505	−0.536	18.8	(0.4)	5.7	(0.3)	2.0	(0.2)	37.1	(0.4)
Car 2	10	287.555	−0.536	13.0	(0.5)	3.3	(0.2)	0.8	(0.1)	33.0	(0.4)
Car 2	11	287.605	−0.536	15.2	(0.3)	5.8	(0.4)	0.8	(0.1)	33.6	(0.4)
Car 2	12	287.655	−0.536	16.7	(0.5)	5.8	(0.3)	1.4	(0.1)	32.2	(0.4)
Car 2	13	287.405	−0.486	20.7	(0.5)	2.9	(0.2)	1.1	(0.1)	38.4	(0.5)
Car 2	14	287.455	−0.486	12.9	(0.4)	3.3	(0.3)	0.8	(0.1)	32.9	(0.5)
Car 2	15	287.505	−0.486	27.6	(0.6)	5.8	(0.3)	1.5	(0.1)	42.1	(0.4)
Car 2	16	287.555	−0.486	17.7	(0.3)	3.7	(0.2)	1.0	(0.1)	31.4	(0.4)
Car 2	17	287.605	−0.486	14.7	(0.4)	4.2	(0.2)	1.0	(0.1)	28.9	(0.5)
Car 2	18	287.655	−0.486	10.7	(0.4)	3.3	(0.2)	0.8	(0.1)	22.6	(0.3)
Car 2	19	287.405	−0.436	11.1	(0.4)	2.2	(0.2)	0.3	(0.1)	31.8	(0.3)
Car 2	20	287.455	−0.436	14.7	(0.3)	3.5	(0.3)	0.8	(0.1)	30.7	(0.3)
Car 2	21	287.505	−0.436	17.0	(0.5)	3.3	(0.2)	0.6	(0.1)	27.2	(0.3)
Car 2	22	287.555	−0.436	12.4	(0.4)	5.1	(0.3)	0.6	(0.1)	25.2	(0.4)
Car 2	23	287.605	−0.436	11.6	(0.3)	2.2	(0.2)	0.6	(0.1)	23.2	(0.6)
Car 2	24	287.655	−0.436	8.7	(0.4)	3.6	(0.2)	0.7	(0.1)	23.6	(0.3)
Car 3	1	287.006	−0.788	7.2	(0.3)	3.9	(0.1)	0.1	(0.1)	18.3	(0.2)
Car 3	2	287.056	−0.787	12.1	(0.4)	3.3	(0.1)	0.8	(0.1)	21.7	(0.3)
Car 3	3	287.107	−0.786	11.2	(0.3)	4.0	(0.2)	0.8	(0.2)	35.8	(0.4)
Car 3	4	287.156	−0.786	22.6	(0.4)	5.0	(0.2)	1.1	(0.1)	52.9	(0.6)
Car 3	5	287.207	−0.785	25.8	(0.6)	5.1	(0.2)	1.2	(0.2)	41.1	(0.7)
Car 3	6	287.257	−0.784	15.7	(0.3)	9.2	(0.3)	1.1	(0.1)	47.0	(1.5)
Car 3	7	287.006	−0.738	5.4	(0.2)	5.3	(0.2)	0.3	(0.1)	17.3	(0.3)
Car 3	8	287.056	−0.737	6.2	(0.2)	3.4	(0.1)	0.4	(0.1)	22.5	(0.3)
Car 3	9	287.106	−0.736	16.7	(0.3)	4.6	(0.3)	1.3	(0.1)	36.7	(0.4)
Car 3	10	287.156	−0.736	24.3	(0.5)	7.0	(0.3)	1.5	(0.2)	49.4	(0.9)
Car 3	11	287.206	−0.735	25.7	(0.5)	8.2	(0.3)	0.9	(0.1)	56.3	(0.6)
Car 3	12	287.256	−0.737	27.7	(0.5)	11.6	(0.2)	2.0	(0.2)	62.9	(0.7)
Car 3	13	287.005	−0.688	8.1	(0.3)	4.3	(0.1)	0.4	(0.1)	24.2	(0.2)
Car 3	14	287.055	−0.687	7.0	(0.3)	5.5	(0.3)	0.4	(0.1)	26.7	(0.3)
Car 3	15	287.105	−0.686	10.8	(0.4)	5.7	(0.2)	0.9	(0.2)	33.9	(0.3)
Car 3	16	287.155	−0.686	15.7	(0.4)	8.1	(0.4)	1.2	(0.1)	49.2	(1.0)
Car 3	17	287.205	−0.685	42.3	(0.6)	8.7	(0.3)	3.3	(0.2)	70.4	(0.6)
Car 3	18	287.255	−0.687	27.0	(0.7)	10.0	(0.5)	2.5	(0.3)	81.6	(1.2)

**Table 4**  
(Continued)

Raster Beam <sup>a</sup>		Galactic Coordinates <sup>a</sup> (deg)		Line Intensities [ $10^{-8} \text{ W m}^{-2} \text{ sr}^{-1}$ ] <sup>b</sup>							
				(O I) 63 $\mu\text{m}$		(N II) 122 $\mu\text{m}$		(O I) 146 $\mu\text{m}$		(C II) 158 $\mu\text{m}$	
		$l$	$b$	$I$	$(\sigma_I)$	$I$	$(\sigma_I)$	$I$	$(\sigma_I)$	$I$	$(\sigma_I)$
Car 3	19	287.004	−0.638	10.2	(0.3)	2.3	(0.1)	0.7	(0.1)	24.1	(0.4)
Car 3	20	287.054	−0.637	12.9	(0.3)	2.3	(0.2)	0.9	(0.1)	31.3	(0.5)
Car 3	21	287.104	−0.636	11.1	(0.2)	2.8	(0.2)	0.7	(0.1)	32.1	(0.4)
Car 3	22	287.154	−0.636	18.9	(0.3)	2.0	(0.3)	2.0	(0.2)	41.9	(0.6)
Car 3	23	287.204	−0.635	23.5	(0.4)	2.1	(0.3)	1.5	(0.2)	51.5	(1.0)
Car 3	24	287.254	−0.634	34.3	(0.5)	4.8	(0.3)	1.8	(0.2)	77.0	(1.9)
Car 4	1	287.406	−0.787	6.2	(0.3)	3.7	(0.2)	0.2	(0.1)	18.7	(0.3)
Car 4	2	287.456	−0.786	7.7	(0.3)	3.7	(0.2)	0.2	(0.1)	25.4	(0.3)
Car 4	3	287.506	−0.786	21.9	(0.9)	3.6	(0.3)	0.6	(0.1)	26.9	(0.5)
Car 4	4	287.556	−0.786	9.8	(0.4)	3.7	(0.2)	0.7	(0.1)	31.1	(0.4)
Car 4	5	287.606	−0.786	8.3	(0.3)	5.8	(0.3)	0.8	(0.2)	34.8	(0.6)
Car 4	6	287.656	−0.786	12.3	(0.3)	5.2	(0.2)	1.1	(0.1)	39.6	(0.5)
Car 4	7	287.406	−0.736	7.7	(0.4)	6.0	(0.3)	0.6	(0.1)	31.9	(0.5)
Car 4	8	287.456	−0.736	21.1	(0.5)	4.0	(0.3)	1.7	(0.2)	39.4	(0.5)
Car 4	9	287.506	−0.736	9.7	(0.6)	3.5	(0.3)	0.8	(0.1)	24.8	(0.5)
Car 4	10	287.556	−0.736	12.8	(0.5)	5.4	(0.2)	0.7	(0.2)	36.2	(0.5)
Car 4	11	287.606	−0.736	7.5	(0.3)	6.0	(0.2)	0.5	(0.1)	22.4	(0.4)
Car 4	12	287.656	−0.736	25.2	(0.5)	6.8	(0.3)	3.9	(0.3)	55.2	(1.3)
Car 4	13	287.405	−0.686	72.0	(0.8)	13.5	(0.5)	6.6	(0.3)	73.4	(1.8)
Car 4	14	287.455	−0.686	33.7	(1.0)	6.7	(0.4)	3.1	(0.3)	55.9	(0.5)
Car 4	15	287.505	−0.686	15.3	(0.5)	5.1	(0.3)	1.1	(0.1)	34.4	(0.3)
Car 4	16	287.555	−0.686	12.0	(0.6)	9.9	(0.3)	0.9	(0.1)	20.2	(0.3)
Car 4	17	287.605	−0.686	4.7	(0.4)	5.4	(0.2)	0.4	(0.1)	24.1	(0.3)
Car 4	18	287.655	−0.686	24.2	(0.4)	6.8	(0.2)	1.1	(0.1)	41.6	(0.8)
Car 4	19	287.405	−0.637	69.9	(1.4)	16.6	(0.6)	5.8	(0.3)	72.9	(1.3)
Car 4	20	287.455	−0.636	42.2	(0.6)	15.1	(1.3)	2.3	(0.3)	60.2	(1.1)
Car 4	21	287.505	−0.636	8.9	(1.0)	5.3	(0.3)	0.9	(0.1)	31.9	(0.4)
Car 4	22	287.555	−0.636	21.9	(1.5)	14.4	(0.4)	1.4	(0.2)	41.6	(0.4)
Car 4	23	287.605	−0.636	30.8	(9.7)	17.3	(1.9)	1.2	(0.5)	32.1	(0.4)
Car 4	24	287.655	−0.636	10.6	(0.6)	9.2	(0.2)	0.7	(0.2)	38.9	(0.7)
Car 6	1	287.256	−0.737	26.4	(0.4)	12.3	(0.3)	1.5	(0.2)	61.8	(0.7)
Car 6	2	287.306	−0.736	22.8	(0.5)	12.5	(0.3)	1.5	(0.2)	60.5	(0.5)
Car 6	3	287.356	−0.736	12.8	(0.5)	13.4	(0.3)	1.3	(0.2)	58.9	(1.4)
Car 6	4	287.406	−0.736	7.7	(0.6)	5.7	(0.4)	1.1	(0.1)	19.0	(0.3)
Car 6	5	287.255	−0.687	35.1	(0.5)	7.5	(0.4)	2.5	(0.3)	86.4	(1.4)
Car 6	6	287.305	−0.686	53.1	(0.8)	10.7	(0.5)	3.4	(0.4)	115.3	(1.6)
Car 6	7	287.355	−0.686	89.2	(1.4)	22.4	(0.5)	7.3	(0.4)	163.4	(4.2)
Car 6	8	287.405	−0.686	73.5	(1.0)	12.4	(0.5)	6.3	(0.3)	96.2	(1.9)

**Notes.**<sup>a</sup> Coordinates refer to the center positions of the *ISO* beam, as shown in the raster map in Figure 2.<sup>b</sup> Intensity errors ( $\sigma_I$ ) do not include the *ISO* absolute calibration error of  $\sim 20\%$ .**Table 5**  
Density of the Ionized Medium

Raster Beam		Galactic Coordinates (deg)		Electron Density ( $\text{cm}^{-3}$ )		
		$l$	$b$	$n_e$	( $\sigma_{n_e}$ ) lower	( $\sigma_{n_e}$ ) upper
Car 1	5	287.201	−0.583	39	...	88
Car 1	6	287.251	−0.582	18	...	35
Car 1	12	287.250	−0.532	4	...	29
Car 2	3	287.500	−0.583	122	...	...
Car 2	4	287.550	−0.583	23	20	23
Car 2	5	287.600	−0.583	0	...	6
Car 2	6	287.650	−0.583	24	...	50
Car 2	9	287.500	−0.533	30	...	71
Car 2	10	287.550	−0.533	6	...	31
Car 2	11	287.600	−0.533	30	...	71
Car 3	12	287.250	−0.732	103	...	...
Car 3	18	287.250	−0.682	0	...	3
Car 3	23	287.199	−0.632	0	...	15

**Table 5**  
(Continued)

Raster Beam		Galactic Coordinates (deg)		$n_e$	Electron Density ( $\text{cm}^{-3}$ )	
		$l$	$b$		( $\sigma_{n_e}$ ) lower	( $\sigma_{n_e}$ ) upper
Car 3	24	287.249	-0.632	21	...	54
Car 4	7	287.400	-0.734	29	...	65
Car 4	13	287.400	-0.684	5	...	6
Car 4	17	287.600	-0.683	3	...	14
Car 4	18	287.650	-0.683	33	...	65
Car 4	19	287.400	-0.634	0	...	...
Car 4	21	287.500	-0.633	0	...	...
Car 4	22	287.550	-0.633	16	12	13
Car 4	23	287.600	-0.633	79	64	99
Car 4	24	287.650	-0.633	20	...	24
Car 6	2	287.300	-0.734	75	...	121
Car 6	3	287.350	-0.733	30	23	26
Car 6	6	287.300	-0.684	25	24	29
Car 6	7	287.350	-0.683	24	11	12

**Notes.** This table lists density values derived from the 122/205 line intensity ratio (Section 4.2) and which are plotted in Figure 13. The raster beam numbering notation (the left-hand column) matches that of Table 4, but includes only the 27 *ISO* raster positions overlapped by one or more SPIFI raster positions (i.e., only positions at which the 122/205 ratio could be computed). Upper and lower ( $1\sigma$ ) errors are provided when they are constrained. For example, in the first row of the present table,  $n_e = 39 \text{ cm}^{-3}$  is the best-fit value plotted in Figure 13, while the lower error bar would be (unconstrained) at  $0 \text{ cm}^{-3}$  and the upper error bar would be at  $127 \text{ cm}^{-3}$  (error bars are omitted in the figure for clarity).

**Table 6**  
Raster Beam Assignments for the Carina Nebula Sources in Table 2

Region	SPIFI Raster Beams	<i>ISO</i> Raster Beams
Tr 16	138–142, 147–151, 156–167	Car 4:17, 18, 24
$\eta$ Car	31	Car 4:23
Car II	185–188, 194–197, 203–206	Car 2:4 and Car 4:22
Tr 14	9, 18, 29, 40	Car 2:1, 7, 8
Car I	16, 24–28, 34–39, 44–49	Car 4:19 and Car 6:7
GMC	52–137	Car 1:1–24, Car 3:1–24, and Car 6:1, 2, 4, 5

**Notes.** In Table 2 (Section 4.6), the Carina Nebula was divided into six spatial subregions corresponding to the sources Car I and II, Tr 14 and 16,  $\eta$  Car, and the GMC. In the present table, these sources are listed in the first column, while Columns 2 and 3 provide the specific beam positions of the SPIFI and *ISO* rasters which have been assigned to (i.e., which define, for purposes of this paper) the spatial extent of these six sources. The raster beam numbering notations match those of Tables 3 and 4.

## REFERENCES

- Aannestad, P. A., & Emery, R. J. 2003, *A&A*, **406**, 155  
 Allen, D. A., & Hillier, D. J. 1993, *PASA*, **10**, 338  
 Bennett, C. L., Fixsen, D. J., Hinshaw, G., et al. 1994, *ApJ*, **434**, 587  
 Bernard-Salas, J., & Tielens, A. G. G. M. 2005, *A&A*, **431**, 523  
 Blum, R. D., & Pradhan, A. K. 1992, *ApJS*, **80**, 425  
 Boreiko, R. T., Betz, A. L., & Zmuidzinas, J. 1990, *ApJ*, **353**, 181  
 Bradford, C. M. 2001, PhD thesis, Cornell Univ.  
 Bradford, C. M., Nikola, T., Stacey, G. J., et al. 2003, *ApJ*, **586**, 891  
 Bradford, C. M., Stacey, G. J., Nikola, T., et al. 2005, *ApJ*, **623**, 866  
 Bradford, C. M., Stacey, G. J., Swain, M. R., et al. 2002, *Appl. Opt.*, **41**, 2561  
 Brooks, K. J., Cox, P., Schneider, N., et al. 2003, *A&A*, **412**, 751  
 Brooks, K. J., Storey, J. W. V., & Whiteoak, J. B. 2001, *MNRAS*, **327**, 46  
 Brooks, K. J., Whiteoak, J. B., & Storey, J. W. V. 1998, *PASA*, **15**, 202  
 Brown, J. M., Varberg, T. D., Evenson, K. M., & Cooksy, A. L. 1994, *ApJ*, **428**, L37  
 Clegg, P. E., Ade, P. A. R., Armand, C., et al. 1996, *A&A*, **315**, L38  
 Colgan, S. W. J., Haas, M. R., Erickson, E. F., et al. 1993, *ApJ*, **413**, 237  
 Cooksy, A. L., Blake, G. A., & Saykally, R. J. 1986, *ApJ*, **305**, L89  
 Crawford, M. K., Genzel, R., Townes, C. H., & Watson, D. M. 1985, *ApJ*, **291**, 755  
 de Graauw, T., Lidholm, S., Fitton, B., et al. 1981, *A&A*, **102**, 257  
 Deharveng, L., & Maucherat, M. 1975, *A&A*, **41**, 27  
 Dickel, H. R. 1974, *A&A*, **31**, 11  
 Dickel, H. R., & Wall, J. V. 1974, *A&A*, **31**, 5  
 Feinstein, A. 1995, *RevMexAA Conf. Ser.*, **2**, 57  
 Fixsen, D. J., Bennett, C. L., & Mather, J. C. 1999, *ApJ*, **526**, 207  
 Gardner, F. F., Dickel, H. R., & Whiteoak, J. B. 1973, *A&A*, **23**, 51  
 Gardner, F. F., Milne, D. K., Mezger, P. G., & Wilson, T. L. 1970, *A&A*, **7**, 349  
 Gardner, F. F., & Morimoto, M. 1968, *Aust. J. Phys.*, **21**, 881  
 Ghosh, S. K., Iyengar, K. V. K., Rengarajan, T. N., et al. 1988, *ApJ*, **330**, 928  
 Giannini, T., Lorenzetti, D., Benedettini, M., et al. 1998, in *ASP Conf. Ser.* 132, *Star Formation with the Infrared Space Observatory*, ed. J. L. Yun & R. Liseau (San Francisco, CA: ASP), 350  
 Giannini, T., Nisini, B., Lorenzetti, D., et al. 2000, *A&A*, **358**, 310  
 Goicoechea, J. R., Rodríguez-Fernández, N. J., & Cernicharo, J. 2004, *ApJ*, **600**, 214  
 Gry, C., Swinyard, B., Harwood, A., et al. 2003, in *The ISO Handbook, Vol. III: LWS—The Long Wavelength Spectrometer*, ed. T. G. Müller, J. A. D. L. Blommaert, & P. García-Lario (SAI-99-077/Dc, Version 2.1; ESA SP-1262; Noordwijk: ESA), [http://iso.esac.esa.int/manuals/HANDBOOK/lws\\_hb/](http://iso.esac.esa.int/manuals/HANDBOOK/lws_hb/)  
 Habing, H. J. 1968, *Bull. Astron. Inst. Neth.*, **19**, 421  
 Hollenbach, D. J., & Tielens, A. G. G. M. 1997, *A&A*, **35**, 179  
 Hollenbach, D. J., & Tielens, A. G. G. M. 1999, *Rev. Mod. Phys.*, **71**, 173



- Huchtmeier, W. K., & Day, G. A. 1975, *A&A*, **41**, 153
- Hudson, C. E., & Bell, K. L. 2004, *MNRAS*, **348**, 1275
- Israel, F. P., Maloney, P. R., Geis, N., et al. 1996, *ApJ*, **465**, 738
- Kaufman, M. J., Wolfire, M. G., Hollenbach, D. J., & Luhman, M. L. 1999, *ApJ*, **527**, 795
- Kessler, M. F., Müller, T. G., Leech, K., et al. 2003, in ESA SP-1262, The ISO Handbook, Vol. I: ISO—Mission & Satellite Overview, ed. T. G. Müller, J. A. D. L. Blommaert, & P. García-Lario (SAI-2000-035/Dc, Version 2.0; Noordwijk: ESA), [http://iso.esac.esa.int/manuals/HANDBOOK/gen\\_hb/](http://iso.esac.esa.int/manuals/HANDBOOK/gen_hb/)
- Kessler, M. F., Steinz, J. A., Anderegg, M. E., et al. 1996, *A&A*, **315**, L27
- Kharchenko, N. V., Piskunov, A. E., Röser, S., Schilbach, E., & Scholz, R.-D. 2005, *A&A*, **438**, 1163
- Kramer, C., Cubick, M., Röllig, M., et al. 2008, *A&A*, **477**, 547
- Kramer, C., Jakob, H., Mookerjee, B., et al. 2004, *A&A*, **424**, 887
- Larsson, B., Liseau, R., & Men'shchikov, A. B. 2002, *A&A*, **386**, 1055
- Lasker, B. M., Sturch, C. R., McLean, B. J., et al. 1990, *AJ*, **99**, 2019
- Lloyd, C., Lerate, M. R., & Grundy, T. W. 2003, The LWS L01 Pipeline, Version 1, [http://ida.esac.esa.int:8080/hdpdp/technical\\_reports/technote34.html](http://ida.esac.esa.int:8080/hdpdp/technical_reports/technote34.html)
- Maíz-Apellániz, J., Walborn, N. R., Galué, H. Á., & Wei, L. H. 2004, *ApJS*, **151**, 103
- McGee, R. X., & Gardner, F. F. 1968, *Austral. J. Phys.*, **21**, 149
- Megeath, S. T., Cox, P., Bronfman, L., & Roelfsema, P. R. 1996, *A&A*, **305**, 296
- Meixner, M., Haas, M. R., Tielens, A. G. G. M., Erickson, E. F., & Werner, M. 1992, *ApJ*, **390**, 499
- Mizutani, M., Onaka, T., & Shibai, H. 2002, *A&A*, **382**, 610
- Mizutani, M., Onaka, T., & Shibai, H. 2004, *A&A*, **423**, 579
- Negishi, T., Onaka, T., Chan, K.-W., & Roellig, T. L. 2001, *A&A*, **375**, 566
- Oberst, T. E. 2009, PhD thesis, Cornell Univ.
- Oberst, T. E., Parshley, S. C., Stacey, G., et al. 2006, *ApJ*, **652**, L125
- Petuchowski, S. J., Bennett, C. L., Haas, M. R., Colgan, S. W. J., & Erickson, E. F. 1996, *ApJ*, **459**, 181
- Petuchowski, S. J., Bennett, C. L., Haas, M. R., et al. 1994, *ApJ*, **427**, L17
- Poglitsch, A., Krabbe, A., Madden, S. C., et al. 1995, *ApJ*, **454**, 293
- Pound, M. W., & Wolfire, M. G. 2008, in ASP Conf. Ser. 394, Astronomical Data Analysis Software and Systems (ADASS) XVII, ed. R. W. Argyle, P. S. Bunclark, & J. R. Lewis (San Francisco, CA: ASP), 654
- Rathborne, J. M., Burton, M. G., Brooks, K. J., et al. 2002, *MNRAS*, **331**, 85
- Retallack, D. S. 1983, *MNRAS*, **204**, 669
- Röser, S., & Bastian, U. 1988, *A&AS*, **74**, 449
- Salama, A. 2000, in ISO Beyond Point Sources: Studies of Extended Infrared Emission, ed. R. J. Laurejis, K. Leech, & M. F. Kessler (ESA SP-455; Noordwijk: ESA), 7
- Sanchawala, K., Chen, W.-P., Lee, H.-T., et al. 2007a, *ApJ*, **656**, 462
- Sanchawala, K., Chen, W.-P., Ojha, D., et al. 2007b, *ApJ*, **667**, 963
- Savage, B. D., & Sembach, K. R. 1996, *ARA&A*, **34**, 279
- Saykally, R. J., & Evenson, K. M. 1979, *J. Chem. Phys.*, **71**, 1564
- Shibai, H., Okuda, H., Nakagawa, T., et al. 1991, *ApJ*, **374**, 522
- Simpson, J. P., Colgan, S. W. J., Cotera, A. S., et al. 1997, *ApJ*, **487**, 689
- Simpson, J. P., Rubin, R. H., Colgan, S. W. J., Erickson, E. F., & Haas, M. R. 2004, *ApJ*, **611**, 338
- Smith, N. 2006a, *MNRAS*, **367**, 763
- Smith, N. 2006b, *ApJ*, **644**, 1151
- Smith, N., Bally, J., & Walborn, N. R. 2010a, *MNRAS*, **405**, 1153
- Smith, N., Povich, M. S., Whitney, B. A., et al. 2010b, *MNRAS*, **406**, 952
- Stacey, G. J., Geis, N., Genzel, R., et al. 1991, *ApJ*, **373**, 423
- Stacey, G. J., Viscuso, P. J., Fuller, C. E., & Kurtz, N. T. 1985, *ApJ*, **289**, 803
- Stark, A. A., Bally, J., Balm, S. P., et al. 2001, *PASP*, **113**, 567
- Stark, A. A., Chamberlin, R. A., Ingalls, J., Cheng, J., & Wright, G. 1997b, *Rev. Sci. Instrum.*, **68**, 2200
- Swain, M. R., Bradford, C. M., Stacey, G. J., et al. 1998, *Proc. SPIE*, **3354**, 480
- Swinyard, B. M., Burgdorf, M. J., Clegg, P. E., et al. 1998, *Proc. SPIE*, **3354**, 888
- Tapia, M., Persi, P., Bohigas, J., Roth, M., & Gómez, M. 2006, *MNRAS*, **367**, 513
- Tapia, M., Roth, M., Vázquez, R. A., & Feinstein, A. 2003, *MNRAS*, **339**, 44
- Tielens, A. G. G. M., & Hollenbach, D. 1985a, *ApJ*, **291**, 722
- Tielens, A. G. G. M., & Hollenbach, D. 1985b, *ApJ*, **291**, 747
- Tommasi, E., Lorenzetti, D., Giannini, T., Nisini, B., & Palla, F. 1998, *Ap&SS*, **261**, 187
- Unger, S. J., Clegg, P. E., Stacey, G., et al. 2000, *A&A*, **355**, 885
- Vastel, C., Spaans, M., Ceccarelli, C., Tielens, A. G. G. M., & Caux, E. 2001, *A&A*, **376**, 1064
- Walborn, N. R. 1995, *RevMexAA Conf. Ser.*, **2**, 51
- Watson, D. M., Genzel, R., Townes, C. H., Werner, M. W., & Storey, J. W. V. 1984, *ApJ*, **279**, L1
- Whiteoak, J. B. Z. 1994, *ApJ*, **429**, 225
- Wright, E. L., Mather, J. C., Bennett, C., et al. 1991, *ApJ*, **381**, 200
- Yngvesson, S., Gereicht, E., Nicholson, J., et al. 2004, in 15th Int. Symp. Space THz Technology, ed. G. Narayanan (Amherst, MA: Univ. Massachusetts), 365
- Young Owl, R. C., Meixner, M. M., Fong, D., et al. 2002, *ApJ*, **578**, 885
- Zhang, X., Lee, Y., Bolatto, A., & Stark, A. A. 2001, *ApJ*, **553**, 274